creative commons
COMMONS DEED

저작자표시-비영리-변경금지 2.0 대한민국

이용자는 아래의 조건을 따르는 경우에 한하여 자유롭게

- 이 저작물을 복제, 배포, 전송, 전시, 공연 및 방송할 수 있습니다.

다음과 같은 조건을 따라야 합니다:

저작자표시. 귀하는 원저작자를 표시하여야 합니다.

비영리. 귀하는 이 저작물을 영리 목적으로 이용할 수 없습니다.

변경금지. 귀하는 이 저작물을 개작, 변형 또는 가공할 수 없습니다.

- 귀하는, 이 저작물의 재이용이나 배포의 경우, 이 저작물에 적용된 이용허락조건을 명확하게 나타내어야 합니다.
- 저작권자로부터 별도의 허가를 받으면 이러한 조건들은 적용되지 않습니다.

저작권법에 따른 이용자의 권리는 위의 내용에 의하여 영향을 받지 않습니다.

이것은 이용허락규약(Legal Code)을 이해하기 쉽게 요약한 것입니다.

Disclaimer

dCollection

[UCI]I804:21031-200000336749

Thesis for the Degree of Master of Engineering

Predictive Model and Process Optimization for Magnetic Assisted Deburring Using Dynamic Particles

by

Se-Yeong Lee

Department of Mechanical Engineering

The Graduate School

Pukyong National University

August, 2020

Predictive Model and Process Optimization for Magnetic Assisted Deburring Using Dynamic Particles

(자성입자를 이용한 회전 전자기연마에서 버 제거 효과 예측모델 개발 및 공정 최적화)

Advisor: Prof. Jae-Seob Kwak

by

Se-Yeong Lee

A thesis submitted in partial fulfillment of the requirements
for the degree of

Master of Engineering

in Department of Mechanical Engineering, The Graduate School,
Pukyong National University

August 2020

Predictive Model and Process Optimization for Magnetic Assisted Deburring Using Dynamic Particles

A dissertation

by

Se-Yeong Lee

Approved by:

(Chairman) Young-Whan Park

(Member) Tae-Wan Kim

(Member) Jae-Seob Kwak

August 28, 2020

PUKYONG NATIONAL UNIVERSITY 부경대학교

Contents

PUKYONG NATIONAL UNIVERSITY
부경대학교

Nomenclature

a : Minimum value of uniform distribution

A_{debur} : The area of deburring(m^2)

$\overline{B}$: Magnetic flux density(T)

b : Maximum value of uniform distribution

β : Coefficient of regression

B_i : Initial burr height(m)

B_f : Final burr height afterwards on REMF(m)

B_{total} : Total magnetic flux density(T)

χ : Magnetic susceptibility

d : Distance of moment(m)

e_{RSM} : Modeling error

F : Function of x, y

$\overline{F_p}$: Force of magnetic particle(N)

f : Linear function of u and its derivatives

$\overline{H}$: Magnetic intensity(A/m)

h : Height of interest(m)

I : Inertial moment($kg \cdot m^2$)

J : Magnetization(A/m)

K : Kinetic energy(J)

l : Length vector(m)

M : Mass of particles(kg)

$\overline{M}$: Magnetization per unit volume(A/m^3)

$\overrightarrow{M}$: Magnetic vector(A/m)

m : Magnetic dipole moment(A·m^2)

m_{eff} : Effective moment(A·m^2)

μ : Mean of the normal distribution

μ_0 : Permeability of vacuum(H/m)

n : Size of a random sample

w : Angular velocity(rad/s)

R^2 : R-squared

r_H : Relative ratio for burr height

ρ : Density of particle(kg/m^3)

σ^2 : Standard deviation of the normal distribution

SSE : Sum of squares of error

SST : Sum of squares total

$\overline{T_p}$: Moment of a couple(N·m)

$\overline{T_\theta}$: Moment of a couple in tilt magnetic field(N·m)

u : Target value

V : Volume(m^3)

v : Velocity of particle(rpm)

W_{total} : Total weight of particles(kg)

x_i : Input variable

y : Output variable

$\hat{y}$: Output variable of response surface

List of tables

List of figures

List of Photographs

PUKYONG NATIONAL UNIVERSITY
부경대학교

자성입자를 이용한 회전 전자기연마에서 미세 버 제거 효과 예측모델 개발 및 공정 최적화

이 세 영

부 경 대 학 교 대 학 원 기 계 공 학 과

요 약

산업 발전의 추세에 따라 초정밀 미세부품에 대한 요구가 증가하고 있다. 그러나 모든 가공품은 절삭 과정에서 필연적으로 버가 형성되고, 이로 인하여 기계의 수행 능력과 효율이 저하되는 치명적인 결함을 유발한다. 특히 최근 복잡한 자유형상을 가지는 고기능성 제품의 수요가 증가하면서 정형화된 공구를 사용하는 과거 방식에서 벗어난 새로운 기계적 표면처리법을 통한 디버링 연구의 필요성이 강조되고 있다.

따라서 본 논문에서는 연마입자의 유동성을 활용하여 효과적인 버 제거 및 표면 개선효과를 나타내는 회전 전자기연마공정을 제시하고 상세히 다루고자 한다. 회전 전자기연마가공은 영구자석의 자기 및 운동 특성에 의해 발생하는 복합에너지를 사용하여 자성입자를 가공범위에서 교반시키고, 운동하는 자성입자와 시편간의 충돌을 통해서 불필요한 형상을 제거하는 기술이다.

회전 전자기연마가공의 우수한 효과에도 불구하고 해당 공정에 주요한 연마입자의 운동 특성에 관한 분석이나 효율을 높이기 위한 연구가 부족한 실정이다. 그래서 본 논문에서는 유한요소기법을 활용하여 단일 및 다수 입자의 가공효과를 예측하고 반응표면법을 통한 공정 최적화를 수행하였다.

먼저 충돌해석을 이용하여 디버링 효과를 분석하였다. 회전 전자기연마가공에서 버의 파단을 일으킬 수 있는 항복강도 276 MPa 값을 기준으로 단일 자성입자 충돌로 인한 유효 응력 면적을 분석하였다. 입자의 충돌속도와 지름이 증가하였을 때 운동량이 더 크고 입자의 정렬각도가 클수록 응력이 집중되어 더 넓은 유효 면적이 나타나는 것을 확인하였다. 회전 전자기연마공정에 대해 실제와 유사하게 접근하기 위해서 단일 입자의 해석 결과를 바탕으로 다수 개의 자성입자의 디버링 효과를 산출하였다.

다수 개 자성입자의 충돌해석에서 각 공정인자와 수준에 따른 디버링 면적을 분석한 결과, 입자의 충돌속도 33 m/s, 총 중량 2.0 kg, 지름 0.7 mm일 때 최대 2.38 mm^2의 값을 얻는 것을 확인하였다. 그리고 시뮬레이션 결과를 바탕으로 다항식 회귀모델을 이용하여 디버링 면적에 대한 예측모델을 제시하고 연속적인 반응을 분석하여 최적화를 수행하였다. 제시된 예측모델은 약 95%의 적합도를 보였으며 약 83%의 예측 정확도를 나타내었다. 모델을 이용하여 도출된 최적 공정조건은 실제 시뮬레이션을 통한 최적 조건과 동일하게 나타나고 예측 면적값이 2.27 mm^2으로 약 95% 유사하여 개발된 예측모델이 충분한 신뢰성을 가짐을 확인하였다. 그리고 동일한 조건에서 실제 실험을 수행하여 최적 공정조건 입자의 회전속도 1,800 rpm, 총

중량 1.5 kg, 지름 0.7 mm을 확인하였다. 두 최적 조건을 비교해본 결과, 실제 실험에서 입자의 상호충돌로 인해 디버링 효과가 저해되어 총 중량 요인에서 약간의 차이가 존재하였다. 하지만 입자의 속도와 지름에 관여하는 요인의 최적 수준이 동일하고 각 운동특성의 주효과 경향이 유사하며 가장 영향력이 큰 인자가 총 중량으로 동일하였다. 그래서 제시된 수치적 접근법이 회전 전자기연마공정의 연마특성 규명에 적합함을 알 수 있었다.

PUKYONG NATIONAL UNIVERSITY
부경대학교

1. Introduction

1.1 Research background

As demand for miniaturized products has increased in a wide array of areas such as the automotive, aerospace, electronics, and medical industries, precision engineering plays a crucial role in the micro and nano scaled manufacturing[1~2]. However, in mechanical machining process, undesired burr on the surface was generated inevitably. This phenomenon results in decreasing assemble quality and surface integrity as well as increasing product cost.

In order to remove undesired parts on surface and achieve fine surface with high quality of products, traditional techniques such as honing, lapping, and grinding are widely applied, but it has difficulty in producing micro and nano level finish on difficult-to-machine materials and complex geometries due to rigid tools[3~5]. To overcome the limitations and improve a surface quality, many researchers have tried to develop advanced finishing technologies.

Among the various developed finishing processes, abrasive finishing which includes abrasive flow finishing(AFF)[6~8], magnetic abrasive finishing(MAF) [9~12], and magnetic abrasive flow finishing(MAFF)[13], is one of the successful methods for small precision components on freeform surface. These processes using micro sized particles are able to control shape of tool flexibly, so it shows better finishing performance with less defects on small-scaled complex surface compared to conventional finishing. However,

these processes are limited in mass production due to low productivity, higher machining cost, and non-uniform abrasive force[14~17].

Thus, this paper suggests rotational electro-magnetic finishing(REMF) as a novel abrasive finishing process to address drawbacks of aforementioned finishing methods. REMF employs impact effects of micro particles affected by the magnetic and the kinetic properties with a relatively simple structure. The interaction between particles and workpiece removes micro-sized burr and it could obtain superior figures. Since it produces large capacity within a container volume at once, it could be efficiently applied to wide range of industries regardless of shapes, materials, numbers, and sizes[18]. Recently, few studies have investigated the effect of REMF on deburring and surface improvement, but it was conducted by an experimental approach only. Thus in this study, numerical analysis using finite element analysis(FEA) would be adopted to analyze abrasives behavior which is a critical influence on deburring performance in the presence of the magnetic field.

1.2 Literature review

The abrasive processes using micro particles have been investigated to obtain desired geometries with high efficiency for micro parts in past decades[19~21].

Gorana et al.[22~23] developed an analytical predictive model for AFM with consistency of experimental outcomes. Seifu et al.[24] proposed simulation for AFM based on the computational fluid dynamic results.

Yamaguchi and Shinmura[25] and Ghang et al.[26] applied MAF to the inner surface using a rotation system of poles and tubes, respectively. Ko et al.[27] investigated an influence of each parameters. And the deburring effect was analyzed to improve a productivity and an accuracy. Mulik et al.[28] integrated the ultrasonic vibration with MAF. Then, interaction of abrasive grains with a target surface was enhanced, as well as the better characteristic was obtained at the optimal condition. Kumar et al.[29] optimized MAF performance to predict the removal burr ratio using a response surface method and a central composite design.

Wani et al.[30] suggested MAFF, which combined with AFF and MAF. And the magnetic distribution associated with the finishing action was examined by a finite element model. Singh et al.[31] carried out an analysis of the performance for MAFF by means of the experiment design and statistical methodology to improve process efficiency and figure out the optimal operating condition.

And other finishing was conducted to improve a surface roughness. Furuya et al.[32] proposed a magnetic polishing using a couple of rotating

magnets and mixed liquid with compounds and clusters. Azami et al.[33] was established advanced mechanism using the stirring-chamber. This rotational flow associated with experimental factors exerted an abrasive media and reduces a surface roughness.

These precious studies generally performed experiments and simulations to verify the influence of abrasive finishing on the surface integrity. However, it is difficult to analyze abrasives' behavior and identify the significance of each parameter affecting process efficiency. Because experimental results include complexities due to uncontrolled environments. In addition, conducted simulations are limited to deductions based on evaluations of flow or magnetic distribution during finishing operation. For the reasons, new predict model is needed, which immediately regards the most dominant parameter in an efficient method.

PUKYONG NATIONAL UNIVERSITY
부경대학교

1.3 Significance and objectives of research

In the recent years, most of previous studies focused on the effect of abrasive finishing on improving surface integrity and deburring by means of the experimental approach. Although some research papers clarified that advanced finishing processes are the useful methods to evaluate whether the process are efficiency for clean surface, it had still problems in terms of cost, productivity, and efficiency. Moreover, it is not sufficient to explain behavior of abrasive particles during operation.

Therefore in this study, REMF is proposed and analyzes mechanism by the simulated approach.

Process efficiency of REMF is directly affected by impact effects of particles, since it utilizes collisions between dynamic particles and workpiece. To verify dynamic characteristics of particles, stress distributions resulted in the interaction between single particle and surface are obtained using explicit simulations. Considering parameters of multi-particles, deburring area are calculated based on the stress values over yield point.

Predictive model for the deburring area is developed by the second-order polynomial regression. And process factors are optimized to increase process efficiency using the response surface. Experiments are performed and optimized in the identical conditions. The simulated and experimental optimal conditions are compared with each other. Consequently, the numerical approach is clear as the reliable method with the acceptable results.

The detail construction of this study is illustrated as Fig. 1.1.

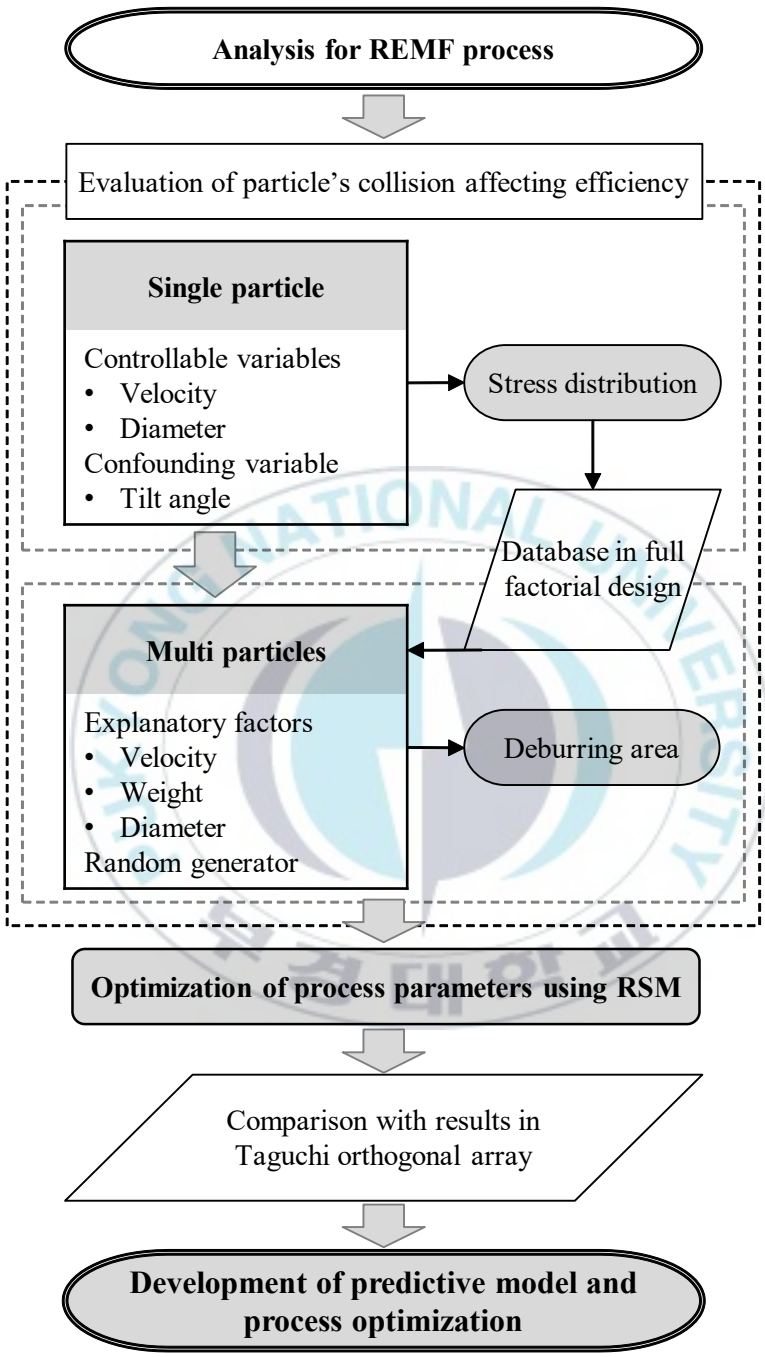

Fig. 1.1 The flow chart for this study

2. Theoretical background

2.1 Rotational electro-magnetic finishing

2.1.1 Mechanism of rotational electro-magnetic finishing

REMF is combined with magnetic and kinetic energy. Both energy help to move magnetic particles to eliminate burrs formed on edges and enhance surface quality.

The schematic apparatus of REMF is shown in Fig. 2.1 and it is divided into 3 parts as container, magnetic, and motor control parts.

The container part is the place to perform the deburring process. There is a large cylinder with 720 mm of diameter, which contains magnetic particles as a tool in REMF, liquid, and workpiece. The behavior of magnetic particles dominantly affected by magnetic force induced from the permanent magnets in the magnetic part during the process. The movement hits the surface and sharp edges to get rid of unwanted materials. The liquid is mixed with polishing compounds and water. It could help to prevent getting too much heat and to burnish a surface of specimen. The magnetic part has permanent magnets embedded in a round plate. Magnets provide the significantly strong magnetic field. In addition, the motor control part is mechanically connected with the round plate.

The round plate rotates along the perpendicular axis when AC motor operates. Simultaneously, permanent magnets turn around in a circle and create the rotating magnetic field. Force and toque induced by the mobile

magnetic field are exerted on magnetic particles. As the result, the effective movement of magnetized particles repeatedly collides with workpiece in REMF. Hence, this novel process improves a surface roughness and eliminates a burr.

PUKYONG NATIONAL UNIVERSITY
부경대학교

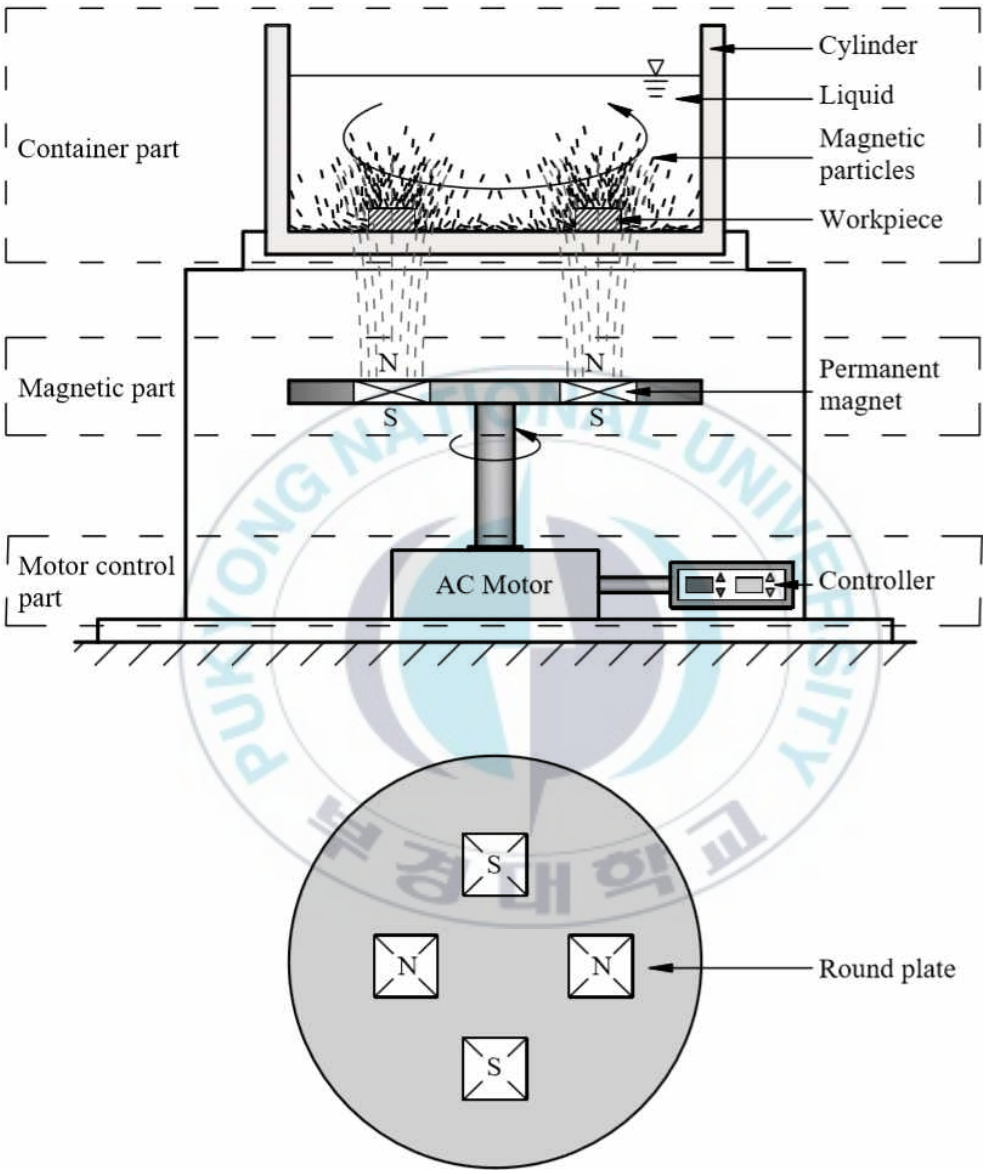

Fig. 2.1 Schematic apparatus of REMF

2.1.2 Motion on a single magnetized particle

The mechanism of REMF is different with a conventional finishing, since the complex energy leads to moving a magnetic particle as a flexible tool in the presence of the alternating magnetic field. Magnetizable particles experience magnetization in the arbitrary uniform magnetic field. The magnetization of a body along the magnetic vector($\vec{M}$) can be always decomposed into a directional magnetic component. However, this paper considers the 1 dimensional motion only, which is perpendicular to the target plane.

When the magnetic particle is suspended in a magnetically linear liquid of permeability and subjected to an almost uniform magnetic intensity($\overline{H}$) in a tiny volume, the relationship is defined as Eqs. (2.1) and (2.2)[34~35].

$$\overline{B} = \mu_0(\overline{H} + \overline{M}) = \mu_0 H + J \tag{2.1}$$

$$J = \mu_0 \overline{M} \tag{2.2}$$

where $\overline{B}$ is a magnetic flux density, μ_0 called the permeability of vacuum is $4\pi \times 10^{-7}$ N/A, $\overline{M}$ is the magnetization of particle per unit volume, and J is a magnetization value.

When the magnetic material is linear and isotropic, Eqs. (2.1) and (2.2) are written as Eqs. (2.3) and (2.4).

$$\overline{B} = (\mu_0 + \chi)\overline{H} = \mu \overline{H} \tag{2.3}$$

$$J = \chi H = \frac{\overline{M}}{V} = \frac{ml}{V} \tag{2.4}$$

where χ is the magnetic susceptibility of a particle, V is the volume of a particle, m is the magnetic dipole moment, and l is the length of a separate vector.

Because of the magnetization, the particle is exploited by the magnetic force and the moment of a couple defined as Eqs. (2.5) and (2.6)[34].

$$\overline{F_p} = m_{eff} \bullet \nabla \overline{H} = \chi V \overline{H} \bullet \nabla \overline{H} \tag{2.5}$$

$$\overline{T_p} = \frac{\overline{d}}{2} \times m\overline{H} - \frac{\overline{d}}{2} \times (m\overline{H}) = \chi V \overline{H} \times \nabla \overline{H} \tag{2.6}$$

where $\overline{F_p}$ is the force of a magnetic particle, m_{eff} is an effective moment, $\overline{T_p}$ is the moment of a couple, and d is a distance of the moment.

In REMF process, the magnetic material revolves around an axis of magnet's circle by $\overline{F_p}$. In addition, the magnetic body is influenced by a couple of $\overline{T_p}$ at each pole. When the magnetic axis of the particle is inclined at the certain angle(θ) in the magnetic field, the body adjusts its axis parallel to the axis of the magnetic field. A couple of moment($\overline{T_\theta}$) are adopted to rotate the magnetic axis at each pole as given in Eq. (2.7)[36~37].

$$\overline{T_\theta} = mlH\sin\theta \tag{2.7}$$

where l is the distance between each pole.

The dynamic particle exhibits the motion of rotation and revolution. Therefore, the kinetic energy of the body can be calculated by sum of translation and rotation energy as defined in Eq. (2.8)[38].

$$K = \frac{1}{2}(Mv^2 + Iw^2) \tag{2.8}$$

where K is a kinetic energy, M is a mass of particle, v is a velocity of particle, I is an inertial moment, and w is an angular velocity. The inertial moment can be measured as described in Eq. (2.9).

$$I = \frac{1}{12}Ml^2\sin^2\theta \tag{2.9}$$

Fig. 2.2 illustrates the motions by the combined energy during REMF process such as revolution and rotation of the particle. It collides with the surface of workpiece. Hence, the burr, which is the critical defect for an integrity, is removed and the product quality is improved.

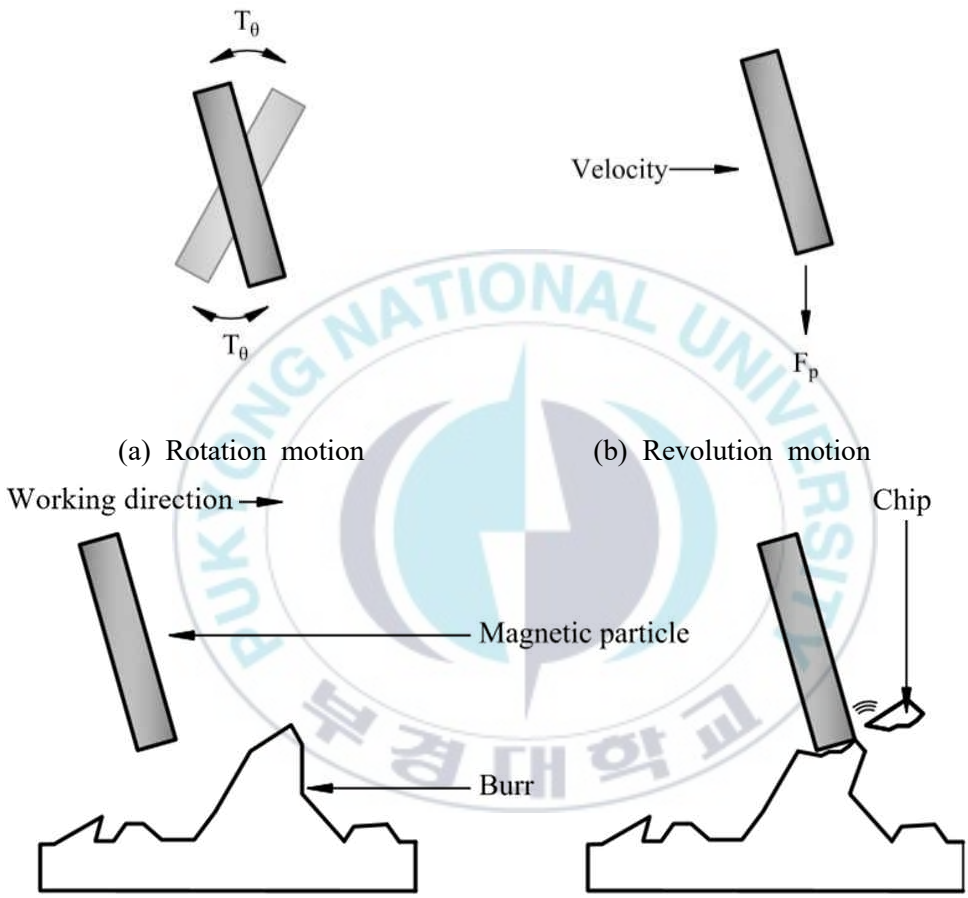

(a) Rotation motion (b) Revolution motion

(c) Deburring motion

Fig. 2.2 The motion of a magnetized particle

2.2 Explicit dynamic analysis

Finite element analysis(FEA) as a numerical problem solving methodology is commonly used in simulations of physical processes. As this method subdivides the overall problems into simpler sub-issues it is able to solve difficulties easily.

The explicit dynamics is efficient to solve the physical problem of short duration events with large material deformations, failure, and interactions between bodies and fluids under nonlinear and transient dynamic forces. Explicit dynamics is used to calculate the state of a given system at a different time from the current time so it requires an additional computation and can be harder to implement. Therefore, smaller time steps are required to maintain stable in an explicit analysis.

All explicit problems is expressed through mathematical time dependent ordinary equations(ODE) and partial differential equations(PDE). It is expressed as Eqs. (2.10) and (2.11), respectively.

$$F(x,y',...,y^{(n-1)}) = y^{(n)} \tag{2.10}$$

$$f(x_1,...,x_n;u,\frac{\partial u}{\partial x_1},...,\frac{\partial u}{\partial u_n};\frac{\partial^2 u}{\partial x_1 \partial x_1},...,\frac{\partial^2 u}{\partial x_1 \partial x_n};...) = 0 \tag{2.11}$$

where F is a function of x, y, and derivations of y. f is a linear function of u and derivatives of u. It finds an approximate solution of PDE as well as of integral equations. The solutions is based either on eliminating the differential equation completely or rendering the PED into an approximating

system of ODE, which are then numerically integrated using standard techniques such as Euler's method, Gaussian method, and others.

Considering these features, all of the experiments employed the explicit analysis to verify the impact energy of particles in a short end time.

2.3 Full factorial design

Design of experiments(DOE) is a planning method to lead a model of system performance before the experiment is performed. One of DOE methods is a full factorial design that it consists of two or more factors with discrete levels. Based on designed factors and levels, this statistic method considers all possible combinations.

This strategy allows illustrating main effects of each factor, as well as effects of interactions between factors on the response variable. It can lead to understanding how the result is changed by factors. Thus, this design is a suitable method for finding an optimal condition. Furthermore, factorial experiments are more efficient than one-factor-at-a-time experiments because it provides more information at similar or lower cost. However, when the number of factors is five or greater, it requires a large number of runs.

In this study, 3 significant factors are designed at 3 levels from minimum effective level to maximum value, which are referred to the fundamental experiment. It required only 27 runs to consider all combination of variables. Hence, the analysis is to attain the optimal process condition based on the full factorial experiments efficiently.

2.4 The probability distribution

Probability density function(PDF) of random variable interprets the relation between a set of possible values randomly given. PDF is used to specify and infer the likelihood of random data within a particular range of values.

2.4.1 The uniform distribution

The uniform distribution is one of PDF. This distribution describes arbitrary outcomes in certain bounds. It is defined with all intervals of the same length where it has equally probable. The bounds are defined by the minimum and maximum values. PDF of the continuous uniform distribution is presented as Eq. (2.12).

$$f(x) = \begin{cases} \frac{1}{b-a} & \text{for } a \le x \le b, \\ 0 & \text{for } x < a \text{ or } x > b \end{cases} \tag{2.12}$$

where a is a minimum value of distribution and b is a maximum value of distribution. The uniform function is equal everywhere except for the 0 measurement points.

2.4.2 The normal distribution

The normal distribution, known as the Gaussian distribution, is one of the most important PDF. It describes how the variables are distributed. Mathematically, the general PDF of the normal distribution is as follows Eq. (2.13).

$$N(x|\mu,\sigma^2) \equiv \frac{1}{\sigma\sqrt{2\pi}} \exp\left[-\frac{(x-\mu)^2}{2\sigma^2}\right] \tag{2.13}$$

where X_1, X_2,...,X_n are a random samples, n is a size of samples, μ is a mean from the population, and σ^2 is a standard deviation from the population.

Fig. 2.3 represents continuous normal distribution as a bell curve. The location and scale parameters of the normal distribution are estimated with μ and σ^2, respectively. μ is also its median, mode, and expectation of the distribution. It shows also a symmetric distribution about μ where most of the sampling data are around the central peak and more frequent in occurrence.

Central limit theorem basically states that the sufficiently large data randomly are generated in a way. When the values do not depend on the variables of the other observations, its probability tends toward a normal distribution approximately. Furthermore, the sampling distribution of the mean is centered at the population mean of the original variable no matter what the shape of distribution. The normal distribution with a large sample

size is well behaved and mathematically tractable due to a theoretical basis, central limit theorem.

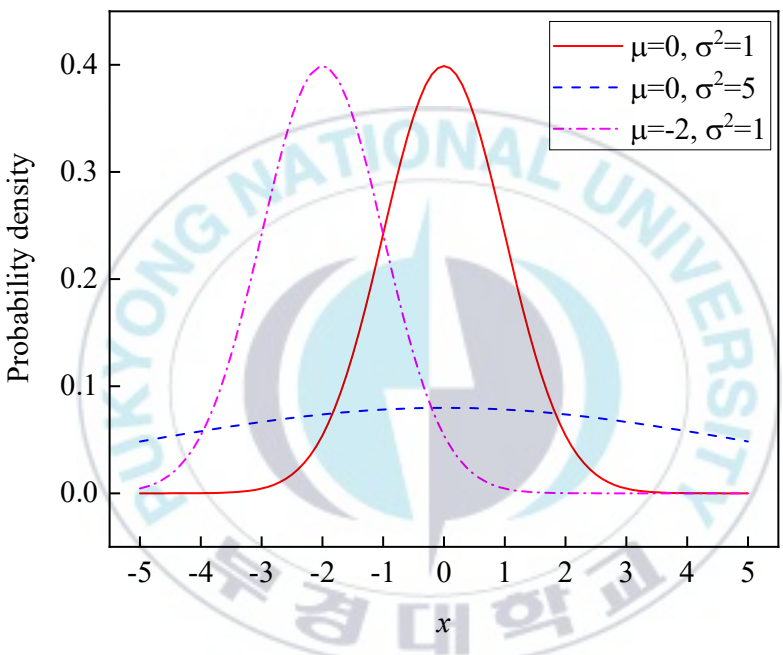

Fig. 2.3 The normal distribution

2.5 The response surface methodology

There are several strategies and models to fit variables in a regression analysis. Some transformations try to keep a regression model of the first order. However, if an influence of independent variables creates a interaction and a square term in two or more variables, techniques of fitting model can be extended to a high degree of the polynomial. The polynomial models can be used to show a nonlinear relationship among explanatory variables.

The response surface methodology(RSM) generally covers the quadratic relation between the input and the output. Performing analysis of RSM provides the characteristics with respect to given parameters. It also has an important capacity to design experiments, to evaluate significant factors, and to develop an optimal operation.

Thus, RSM is adopted to find the influence of characteristics and the desirable condition in this study. RSM is an approximation using the statistical and mathematical approaches. Sometimes a higher order model fails to explain a behavior due to the over-fitting problem. For that reason, the second-order function was employed as defined in Eq. (2.14).

$$\hat{y}= \beta_0 + \sum_{i=1}^{n} \beta_i x_i + \sum_{i=1}^{n} \beta_i x_i^{2+} \sum_{1 \le i < j}^{n} \beta_{ij} x_i x_j \tag{2.14}$$

where $\hat{y}$ is the output variable obtained from the response surface model, β is the regression coefficients, and x_i is the input variable.

The actual output(y) is described as Eq. (2.15).

$$y = \hat{y} + e_{RSM} \tag{2.15}$$

where e_{RSM} is the modeling error.

To represent the error for N data, the sum of squares of error(SSE) is expressed as Eq. (2.16).

$$SSE = \sum_{i=1}^{N} (y_i - \hat{y})^2 = \sum_{i=i}^{N} e_{RSM,y_i^2}^2 \tag{2.16}$$

Moreover, the sum of squares total(SST) is described as Eq. (2.17).

$$SST = \sum_{i=1}^{N} (y_i - \bar{y})^2, \quad \bar{y} = \frac{1}{N} \sum_{i=1}^{N} y_i \tag{2.17}$$

To check of the goodness-of-fit, R-squared(R^2) is defined as Eq. (2.18).

$$R^2 = 1 - \frac{SSE}{SST} \tag{2.18}$$

When R^2 is close to 1, it can express that the model fitting is appropriately performed.

The optimum operating condition for the system is to determine a

stationary point containing the nature of effects. The stationary point is located at the partial derivatives with respect to the x_i and set to 0 as represented in Eq. (2.19).

$$\frac{\partial \hat{y}}{\partial x_1} = \frac{\partial \hat{y}}{\partial x_2} = \cdots = \frac{\partial \hat{y}}{\partial x_k} = 0 \tag{2.19}$$

RSM can be illustrated by 3D surface plots. The graph indicates the intuitive information of the relation.

Particularly, this study estimates the maximum response to enlarge area related to the efficiency of a material removal.

PUKYONG NATIONAL UNIVERSITY 부경대학교

3. Particle dynamics simulation

As mentioned in chapter 2.1, REMF utilizes the impact energy of magnetized particles for fine surface of the workpiece surface by removing rough edges in a very short time interval. In this study, virtual experiments were carried out using FEA which works with less time and cost.

The numerical strategy was devised as shown in Fig. 3.1 to analyze the effect of abrasive process on the morphological characteristics. In REMF process, there were a number of dynamic particles but it was hard pressed to predict kinetic conditions of all particles such as arrangement, tilting angle, and others. Therefore, this study performs the explicit simulations of a single dynamic particle to prove the behavior of kinetic characteristics, first. Based on stress distributions resulted from the single collision, analysis for multi-particles were conducted to verify deburring effect of REMF.

The simulation was concentrated on the interest of volume, 5 mm × 2 mm × 5 mm for effective computing resources. In this virtual model, the center of the volume was also apposed at the radius 180 mm of the cylinder container as shown in Fig. 3.2, because the permanent magnets strongly inducing the magnetic energy were located at the point.

The magnetic particles as the tool in REMF revolved along the axis of the container in the presence of the magnetic field. In the analysis model, the tool movement regard to a linear transportation, because the radial distance from the center of the cylinder to the particle was much longer than the width of the interest volume. Thus, only 1 dimensional collision directed normal to the surface was considered in the dynamic simulations

between magnetic particles and surface of workpiece.

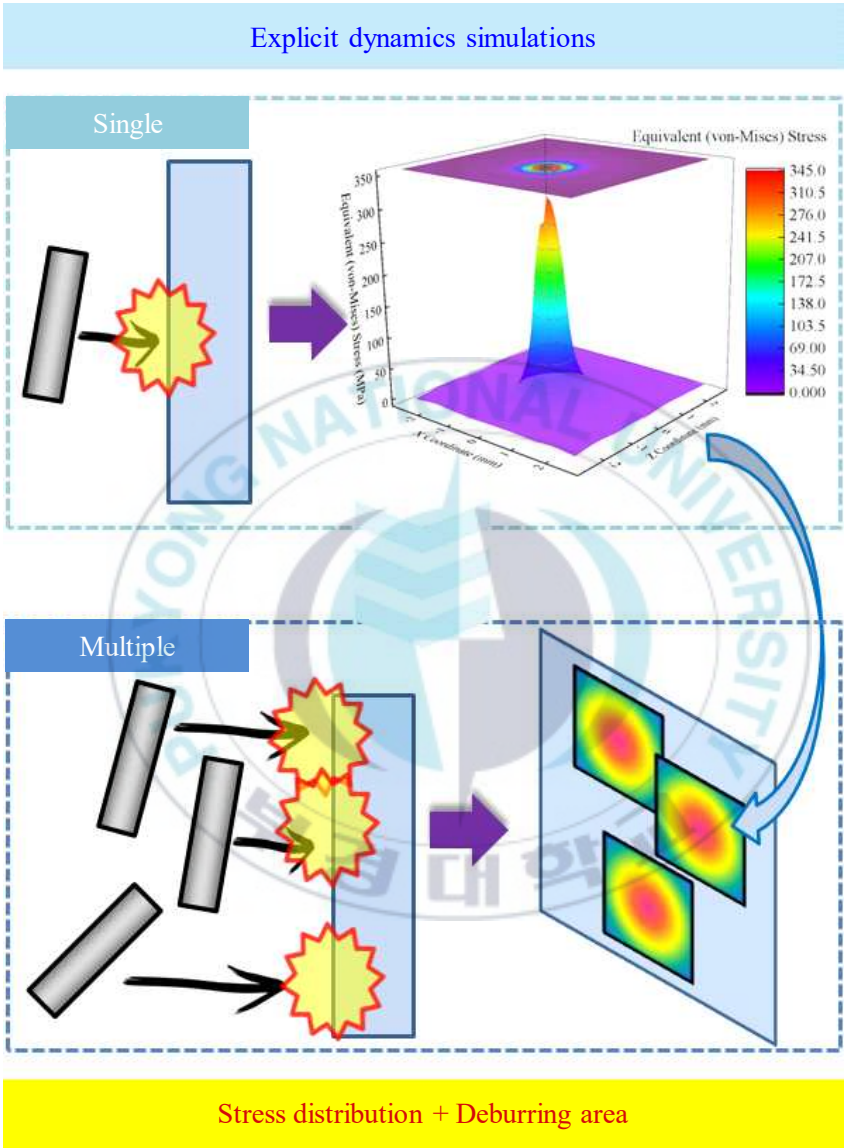

Fig. 3.1 The numerical strategy for REMF

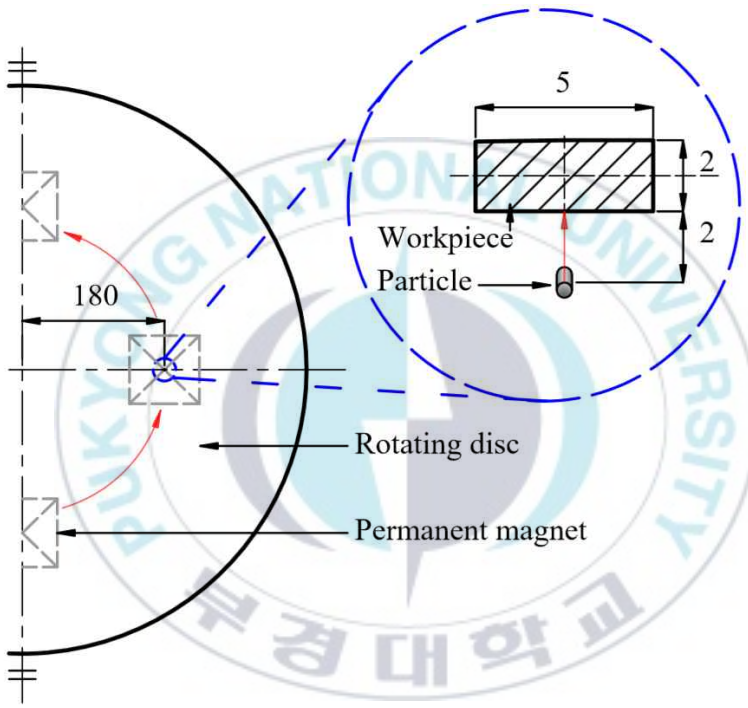

Fig. 3.2 Region of interest in a simulation model

3.1 Single particle simulation

3.1.1 Parameter conditions

Simulations based on dynamic conditions were performed to clarify the collision effect of a single magnetized particle during REMF process using FEA. As stated in chapter 2.2, the movements of a magnetic particle were driven from kinematic and magnetic nature during REMF.

The fixed parameter conditions of a single particle simulation were described in Table 3.1. The initial position between center points of the particle and the workpiece was parallel and the distance was about 2 mm. The end time of simulation was 0.0001 s, which was enough to collide with each other. The materials of the workpiece and the particle were Al6061 and cold finished STS304, respectively. The each material property was shown in Table 3.2[39] and Fig. 3.4. Steinberg Guinan strength model was adopted for the workpiece to calculate the plastic deformation.

In the model, a particle was magnetized and suspended in the magnetic field induced from the permanent magnets. The particle revolving in the radius 180 mm was linearly accelerated to collide with the target surface according to the rotational velocity of the magnets as shown in Fig. 3.3. The particle's velocity in this simulation was calculated by Eq. (3.1).

$$Velocity = \frac{2 \times \pi \times 0.180 \times N}{60} \tag{3.1}$$

where R was the rotational velocity of magnets.

Table 3.3 described the simulated factors and levels of FEA, which significantly affected stress values. The factors and levels were referred to fundamental experiments. The levels of the velocity were calculated based on the rotational velocity of the experimental machine which ranged from the minimum value of 1,200 rpm to the maximum speed of 1,800 rpm. The levels of the diameter were 0.3, 0.5, and 0.7 mm, because the larger diameter caused surface defects due to excessive force. Especially, the tilting angle had a variety of ranges from the parallel to the perpendicular angle to the magnetic line, because the magnetic field was frequently changed in random. The variables were almost equally distributed as denoted in Table 3.3.

PUKYONG NATIONAL UNIVERSITY
부경대학교

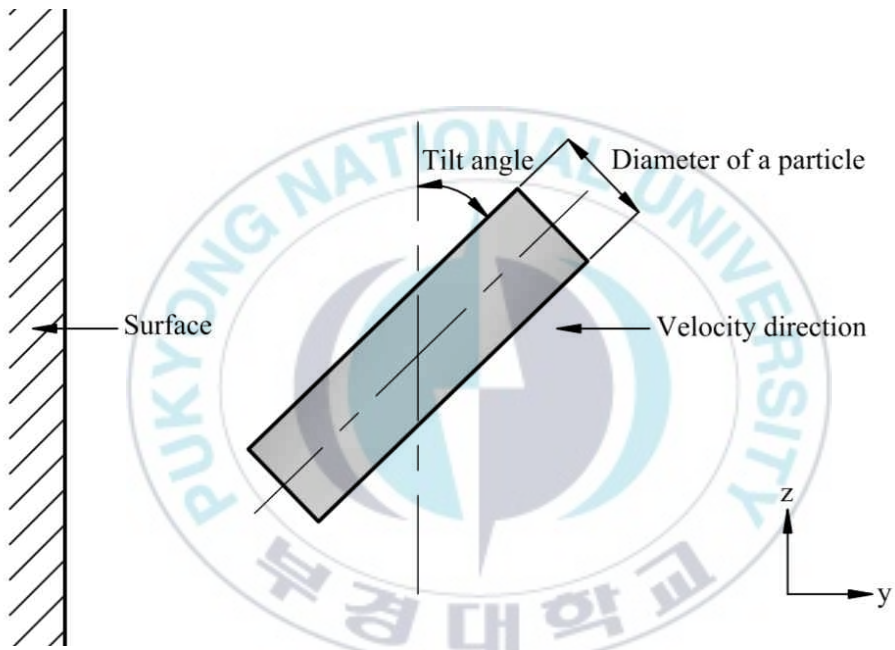

Fig. 3.3 Schematic model of single particle in x and y plane

Table 3.1 Fixed process parameters

Items	Conditions
Located distance from center(mm)	180
Volume of interest(mm^3)	5×2×5
Initial distance(mm)	2
Height of particle(mm)	3
End time(s)	0.0001
Workpiece	Al6061
Particle	STS304

Table 3.2 Properties of Al6061 and STS304

Materials	Mechanical properties	
Al6061	Density(kg/m^3)	2,700
	Shear strength(MPa)	207
	Initial yield strength(MPa)	276
	Maximum yield strength(MPa)	680
	Hardening exponent	0.10
	dG/dP	1.80
	dG/dT(MPa/℃)	-17
	dY/dP	0.019
	Melting temperature(℃)	946.85
STS304	Density(kg/m^3)	8,000
	Yield strength(MPa)	205
	Tensile strength(MPa)	515
	Shear strength(MPa)	77,000
	Poisson's ratio	0.29
	Elongation(%)	40
	Volume magnetic susceptibility	2.20

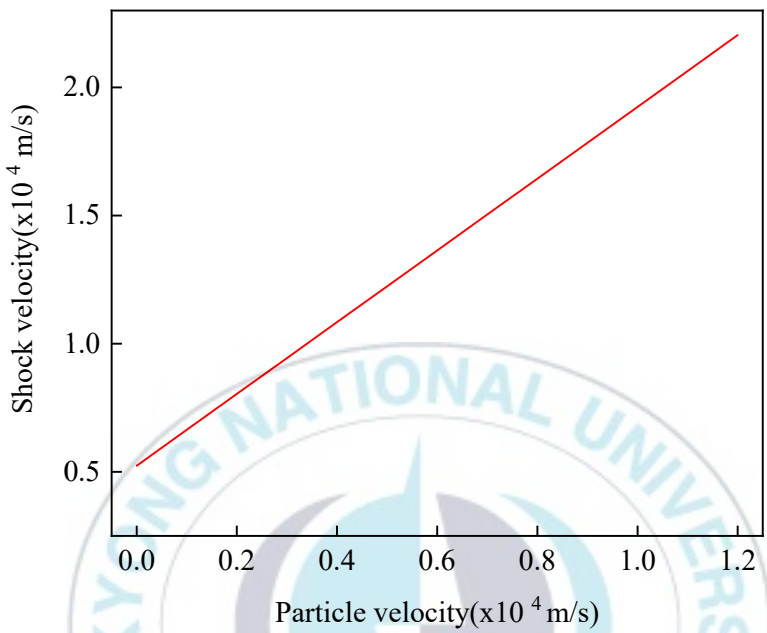

Fig. 3.4 Shock equation of state linear

Table 3.3 Simulated factors and levels of single particle

Factors		Levels		
		1	2	3
Velocity of a particle(m/s)		23	28	33
Diameter of a particle(mm)		0.3	0.5	0.7
Tilt angle of a particle	Type	Uniform distribution		
	Increment(°)	3		
	Range(°)	0~90		

3.1.2 Model of a single magnetized particle

The configurations of the workpiece and the magnetic particle were created considering simulated parameters by using UG NX11(v.11.0, Siemens Inc., Germany) as shown in Fig. 3.5. The meshes of each part were generated by ANSYS Workbench(v.17.0, ANSYS Inc., USA) as represented in Table 3.4. The mesh sizes of the contact surface of workpiece and the magnetic particle which were directly affected finishing performance was 0.1 mm in order to minimize errors and produce continuous stress values with highly reliable information. In addition, the generated mesh size of other area was 0.5 mm.

The particle considered as a rigid body delivered the impulse to transfer the kinetic energy without any deformation during the collision. In contrast, the workpiece was deformed by the interaction with objects.

The number of nodes and elements according to conditions were listed in Table 3.5. The average number of nodes and elements were 14,500 and 12,500, respectively.

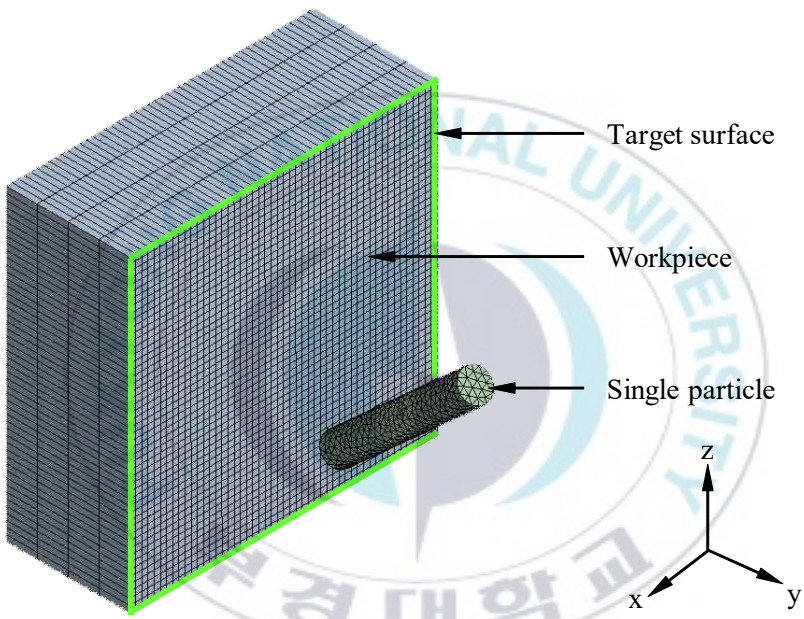

Fig. 3.5 Model of single particle

Table 3.4 Mesh size of single particle

Items	Mesh size(mm)	Type
Workpiece body	0.5	Deformable
Particle body	0.1	Rigid
Workpiece surface	0.1	-

Table 3.5 Nodes and elements of model

Items		Nodes	Elements
Particle	0.3 mm	682	510
	0.5 mm	1,178	5,108
	0.7 mm	2,790	2,370
Workpiece		13,005	10,000

3.1.3 Analysis of a single magnetized particle

The boundary conditions for simulations were shown in Fig. 3.6. The external surfaces of the workpiece were fixed. The initial velocity of a particle was perpendicular to the surface. The gravity and magnetic draw force were considered in z direction due to the magnetic field. The magnetic toque at each angle level was calculated by Eq. (2.7) and applied for the rotation motion in the tangential direction. The engineering software, ANSYS Workbench explicit dynamics, was employed to calculate the physics problem with the large force and a short interval. FEA of 279 cases was performed to analyze the effect of a single object using the full factorial experiment design based on the referred conditions in Table 3.3 and Fig. 3.3.

In order to evaluate the effect of the magnetized particle on removing unexpected parts on the workpiece, the distributions of equivalent von-Mises stress were obtained. Fig. 3.7 showed the number of the elements where the stress value was over the yield stress of Al6061, which was maximum load of 276 MPa without fracture of micro burr thickness. Fig. 3.8 showed comparison results of stress distribution at worst and best condition. As a results, it was noted that the impact energy was directly proportional to the velocity and abrasive diameter. In addition, the stress tended to concentrate with the effective value when the tilt angle increased.

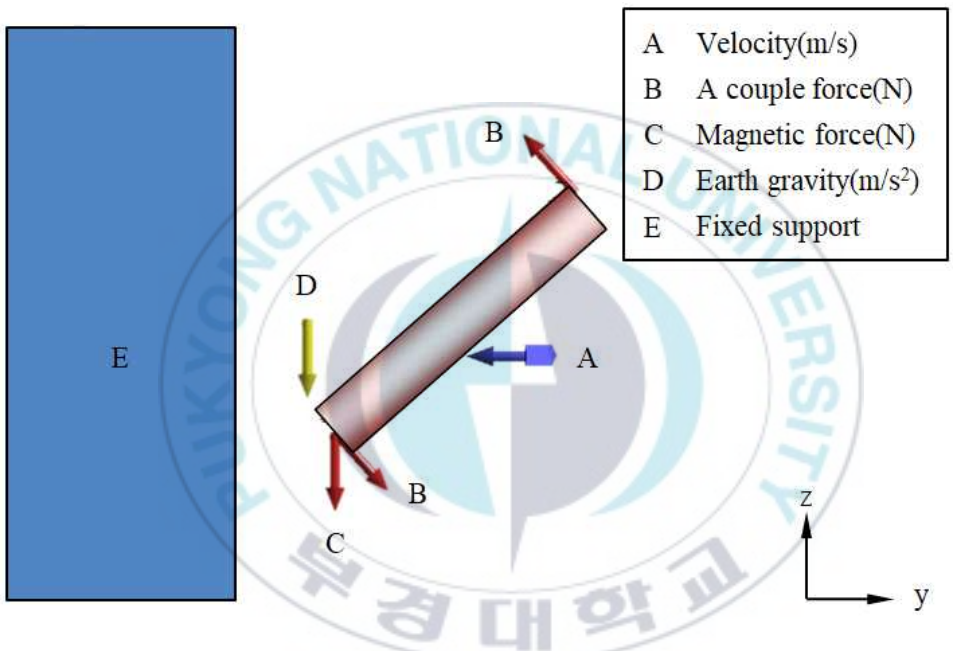

Fig. 3.6 Boundary conditions of a single particle

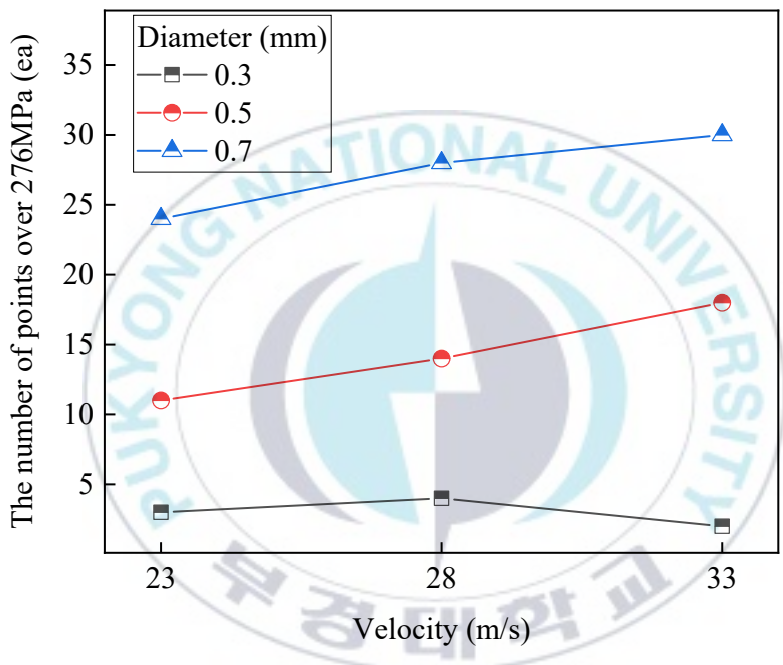

Fig. 3.7 Derived results in single particle simulation for effective stress

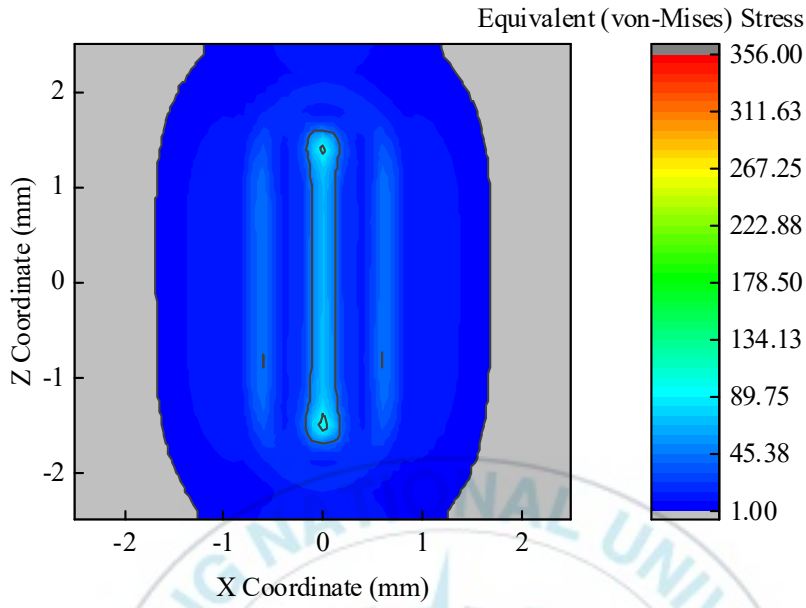

(a) Stress distribution at 23 m/s, 0.3 mm, and 0°

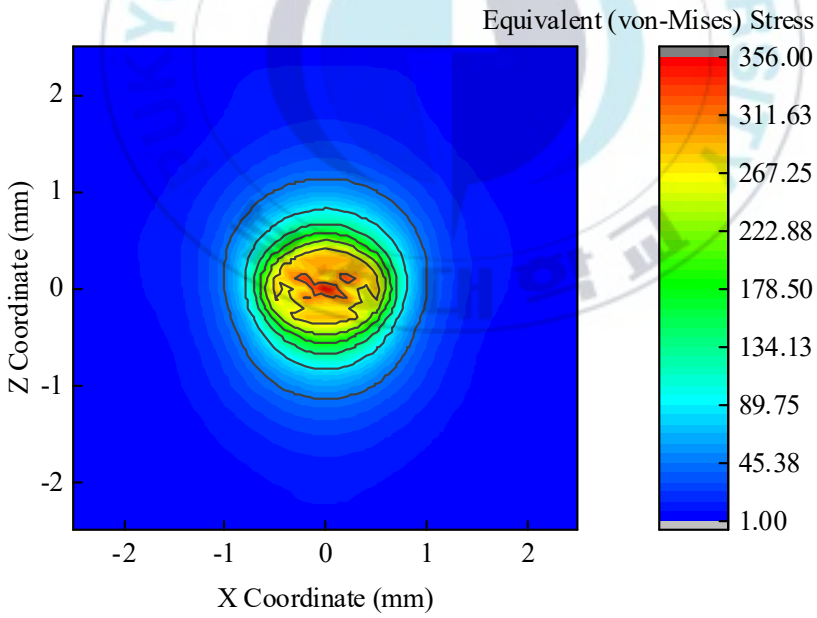

(b) Stress distribution at 33 m/s, 0.7 mm, and 81°

Fig. 3.8 Stress distribution of less and more effective conditions

3.2 Multi-particles simulation

A number of particles independently collided with the deformable body according to the random dynamic characteristics. The results of each single particle were merged in random conditions to obtain the final stress distributions of multi-particles at all factors and levels. These outcomes were acquired and analyzed using full factorial array, which was one of the experimental design methods.

3.2.1 Parameter conditions

Before the analysis of multi-particles, the magnetic particles in the entire container followed the magnetic flux density proportionally. To verify the distribution of magnetic flux density, an electromagnetic simulation was conducted and Fig. 3.9 was obtained. There were 4 magnets alternating the north and south poles at radius 180 mm. Simultaneously, the magnetic flux density had the maximum value of 70.8 mT at the position.

The parameter conditions of multi-particles analysis were illustrated in Table 3.6, which substantially influenced on the effective deburring area. The levels of the particles' velocity and the diameter were identical with the single analysis. On the other hand, the levels of the particles' weight were determined in reference to the results of fundamental experiments. It was 1.0, 1.5, and 2.0 kg, since the heavier weight decreased the process efficiency due to the interaction among the particles. Thus, the investigated variables were designed using full factorial array.

Based on the distribution of the magnetic flux density and the process

parameters, the number of particles was calculated as mentioned in Table 3.7 and Eq. (3.2).

$$N_{A_iC_j} = \frac{W_{total}\, B\, h}{V\, \rho\, B_{total}\, H} \tag{3.2}$$

where W_{total} was the particles' weight and V was the volume of the particle considering the particles' diameter. ρ was the density of the particle, B_{total} was total magnetic flux density, B was the magnetic flux density in the interest domain, H was total height of REMF liquid, and h was a height of the volume of interest.

This analysis assumed that the distribution of magnetic particles followed the uniform probability distribution in the volume of interest, since the magnetic flux density was dense enough and the volume was small enough.

The random generator was organized to specify the anomalous parameters of a particle positions and an angle, as illustrated in the Table 3.8 and Fig. 3.10.

The program created a couple of vectors, which stored information about two directional positions and 1 directional angle separately. The position vector featured a unique set of numbers followed the uniform distribution with the interval of 0.1 mm from -2.5 mm to 2.5 mm. On the other hand, the angle vector was characterized by a repeatable number with the interval of 3° in the range from 0° to 90°. After the vectors were produced, the length of position between new vector and previous ones was compared. If

the measurement was over 0 mm and under the diameter of a particle, the program tried again to generate new sets of vectors. Otherwise, the vectors were saved in the line of the matrix data.

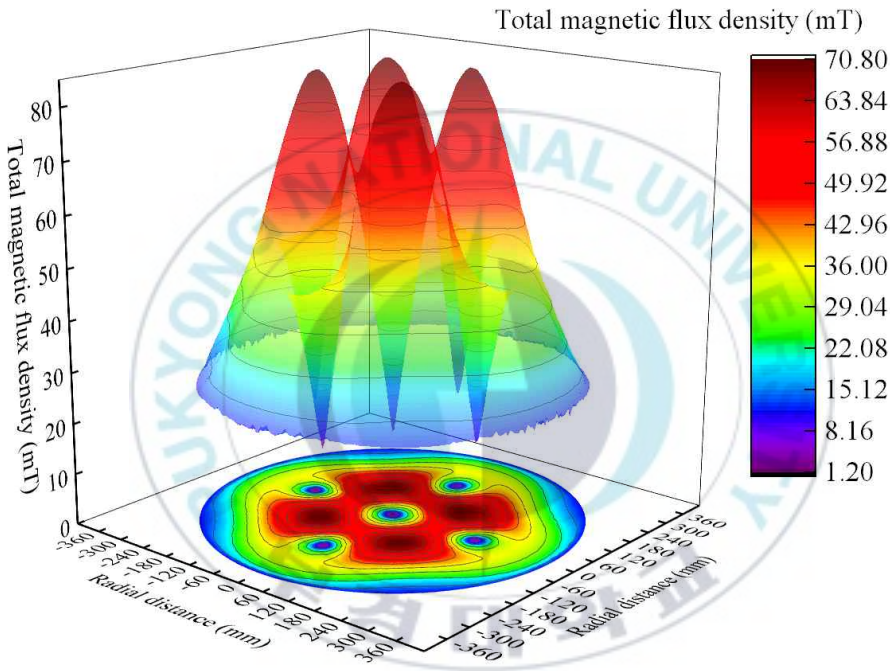

Fig. 3.9 Distribution of magnetic flux density

Table 3.6 Factors and levels of multi-particles

Factors	Levels		
	1	2	3
Velocity of particle(m/s), A	23	28	33
Weight of particles(kg), B	1.0	1.5	2.0
Diameter of particles(mm), C	0.3	0.5	0.7

Table 3.7 The number of the particles considering process conditions

Levels of C	Levels of B		
	1	2	3
1	20	30	40
2	7	10	14
3	3	5	7

Table 3.8 Conditions of random number generation

Factors		Conditions
Position of particles	Directions	2 directions(x, y)
	Range(mm)	-2.5~2.5
	Increment(mm)	0.1
	Type	A set of unique random numbers
Angle of particles	Directions	1 direction(x)
	Range(°)	0~90
	Increment(°)	3
	Type	A repeatable random number

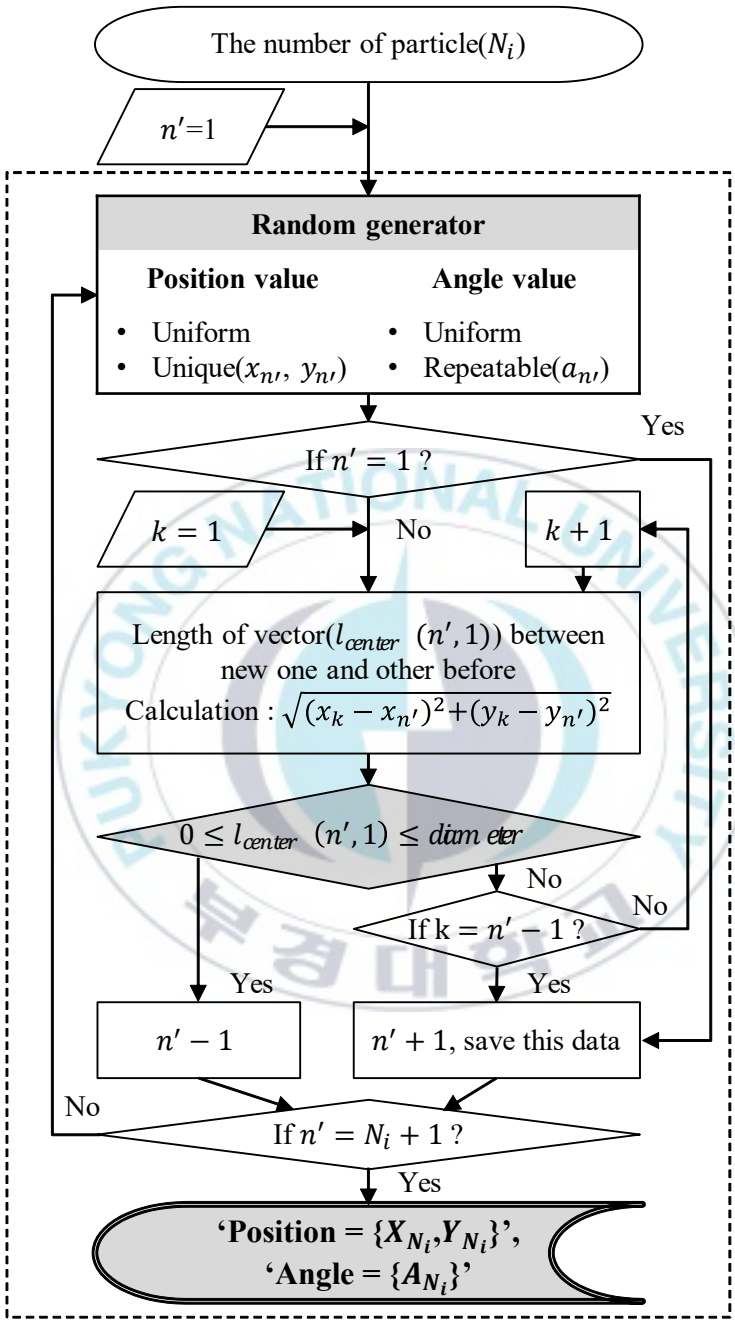

Fig. 3.10 The structure of random numbers generator

3.2.2 Analysis of magnetized particles

The algorithm was proposed for the mathematical approach to analysis of multi-particles as described in the Fig. 3.11. The process was used to integrate the stress distribution matched process parameters and the saved kinetic properties. The numerical computing tool, Matlab R2016a(v.16.0, MathWorks, USA), was adopted to conduct the iterative function.

In consequence of the arithmetic operation, the affected area over certain stress level, about 276 MPa, was defined to evaluate the efficiency of REMF by the response. This was because that the material was permanently deformed over the yield point and the wider machining range was efficient.

The result in the program inevitably contained random errors owing to the random generator. Therefore the numerical analysis was repeated for the accuracy in the sample size of 30 times. It was expressed by the means of the normal distributions referring to the central limit theorem. 27 analyses were conducted at each factor and level. As the results, the mean values were obtained as shown in Table 3.9.

Fig. 3. 12(a) shown the less effective condition at $A_1B_1C_2$ which was 23 m/s of the velocity, 1.0 kg of the weight, and 0.5 mm of the diameter. Deburring area was expected about 0.21 mm^2. On the other hand, Fig. 3.12(b) represented the maximum deburring area of 2.38 mm^2 at $A_3B_3C_3$, corresponding to 33 m/s, 2.0 kg, and 0.7 mm.

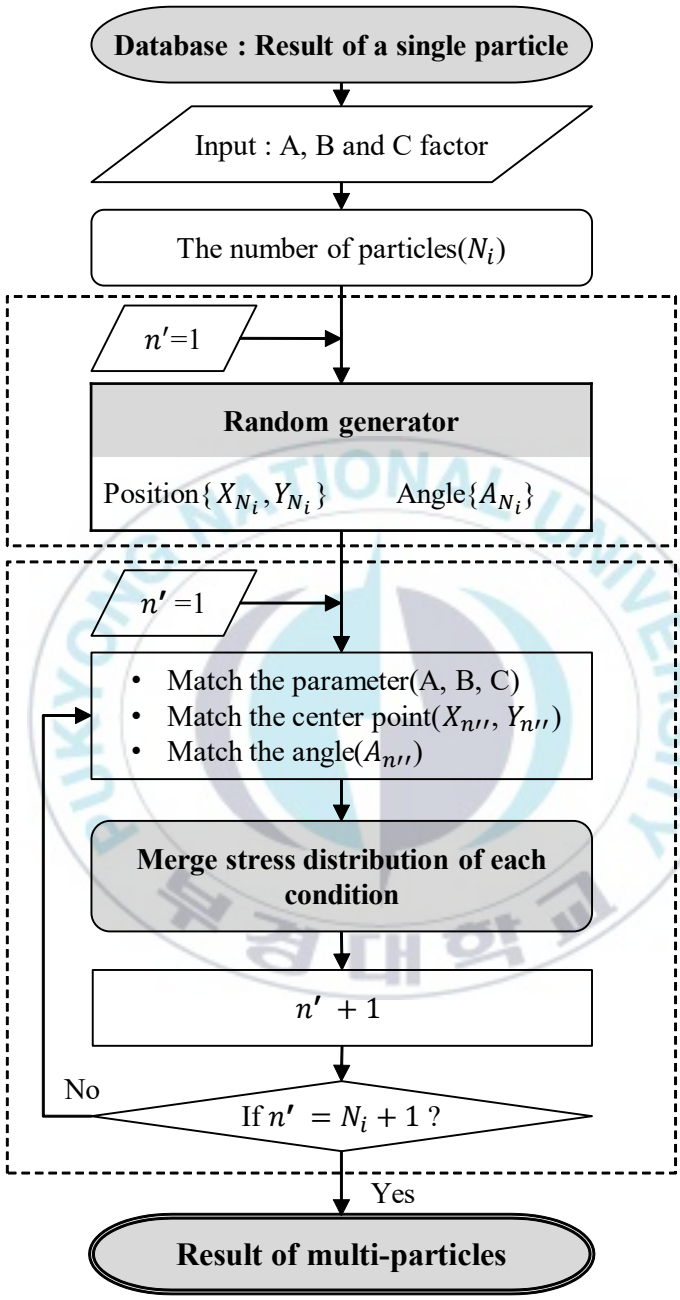

Fig. 3.11 The flow chart for the multi-particles results

Table 3.9 Results of analysis process for multi-particles

Exp. no.	Levels			Means of deburring area(mm^2)
	A	B	C	
1	1	1	1	0.40
2	1	1	2	0.21
3	1	1	3	0.38
4	1	2	1	0.73
5	1	2	2	0.51
6	1	2	3	0.85
7	1	3	1	0.87
8	1	3	2	0.67
9	1	3	3	1.22
10	2	1	1	0.38
11	2	1	2	0.20
12	2	1	3	0.34
13	2	2	1	0.92
14	2	2	2	0.58
15	2	2	3	1.32
16	2	3	1	1.57
17	2	3	2	0.96
18	2	3	3	1.72
19	3	1	1	0.41
20	3	1	2	0.33
21	3	1	3	0.55
22	3	2	1	1.20
23	3	2	2	1.04
24	3	2	3	1.37
25	3	3	1	2.37
26	3	3	2	1.66
27	3	3	3	2.38

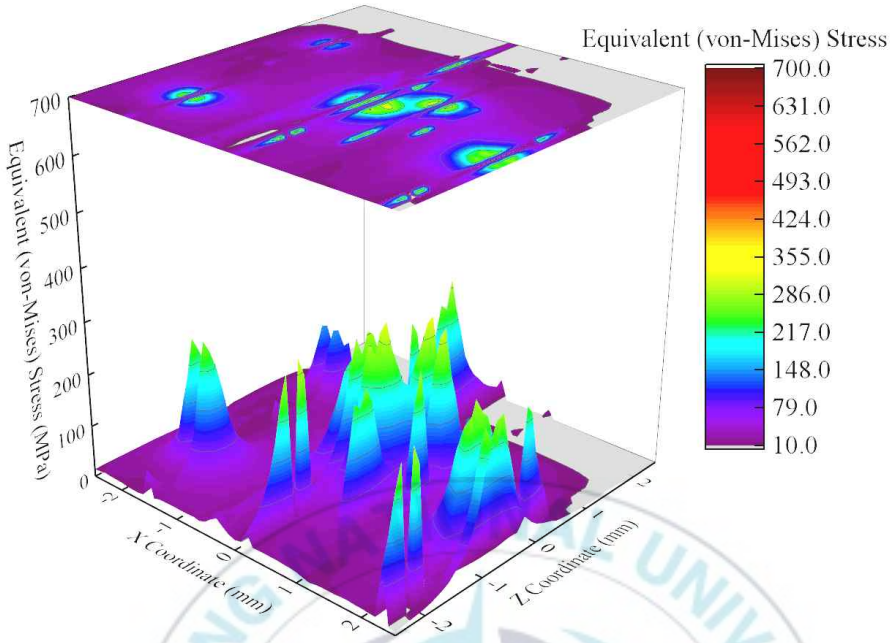

(a) The stress distribution at 23 m/s, 1.0 kg, and 0.5 mm

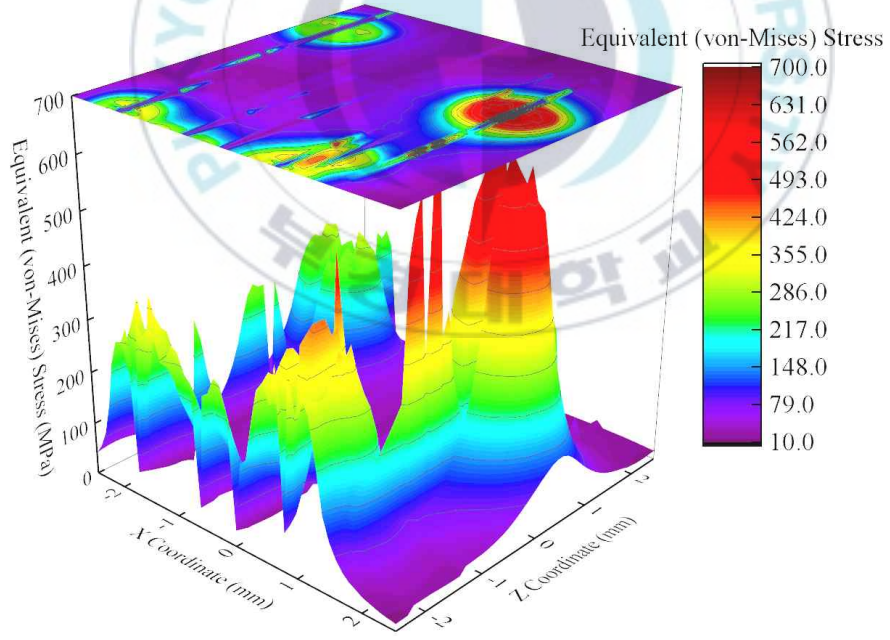

(a) The stress distribution at 33 m/s, 2.0 kg, and 0.7 mm

Fig. 3.12 The stress concentration at the less and more effective conditions

4. Evaluation and optimization of results

4.1 Estimation of characteristics and process optimization

The process optimization was executed to evaluate the larger area associated with the impressive performance. And the significance of factors was evaluated to analyze the data in 3 variables using RSM and analysis of variance(ANOVA). The estimation of the obtained results was carried out using the statistical software Minitab(v.19.0, Minitab Inc., USA).

A second-order polynomial regression model was employed in order to consider interactions and square terms. The pareto chart indicated which the standardized effect are significant at 95% confidence level as shown in Fig. 4.1. According to the analysis, the significant factors of the expected area were B factor of the particles' weight, A factor of the particles' velocity, interaction between A and B factor, square of C factor of the particles' diameter, and C factor.

A main effect plot described differences between means of factors and levels as drawn in Fig. 4.2. As seen in the plot, the influence was larger in the sequence of B, A, and C factor. Especially, C factor was fitted to the curvilinear regression of second-order.

An interaction plot showed the relationship between all possible combinations of explanatory variables as displayed in Fig. 4.3. Only the reaction between A and B factor was closely crossed.

After pooling and revising the explanatory variables, the final regression model for the deburring area was defined as Eq. (4.1).

$$A_{deburr} = 1.40 - 0.25A + 0.01B - 1.41C + 0.37C^2 + 0.28AB \qquad (4.1)$$

where A_{deburr} is the deburring area where the stress value was over 276 MPa.

The statistical significance of the variation was interpreted at a significant level, P-value<0.05, using ANOVA. ANOVA was drawn in Table 4.1. The P-values proved that the influence of A, B, and C factor was significant for the differences. The square term of C factor also was a significant difference affecting the deburring area, as well as the interaction term between A and B factor.

The most important condition, B factor of weight, and it was proportional to the levels. This was because that the number of particles colliding with the surface directly affected the process efficiency. In case of velocity as A factor, the trend of improving surface status was identical as B factor. This was because the kinetic momentum was bigger according to increasing velocity due to Newton's second law of motion. Hence, the interaction between A and B was considered for the kinetic property of the collision. In addition, at the high level of C factor, the impact effect was strong because of the large mass whereas there were a small amount of particles at the same level of the weight. Therefore, the influence of C factor had a curved relation in range of this study.

R^2 of the model was 95.7%, validating the data in good-agreement with

the measurements. The accuracy rate of the predictive values was about 83.3%. Thus, the regression model was fitted to the sample data reasonably as shown in Fig. 4.4.

The response surface optimization was performed to classify the relation and find a maximum operating condition. The predictive model was visualized by 3D response surface plots. Fig. 4.5 illustrated the desired values for the relations of two factors keeping the third constant at its middle levels. As a consequence, the maximum stationary point located at the best combination of $A_3B_3C_3$, which was 33 m/s of the velocity, 2.0 kg of the weight, and 0.7 mm of the diameter. The determined optimal value was 2.27 mm^2 in the predictive model. Compared to the numerical result, about 2.38 mm^2, the overall desirability reached around 95.4%.

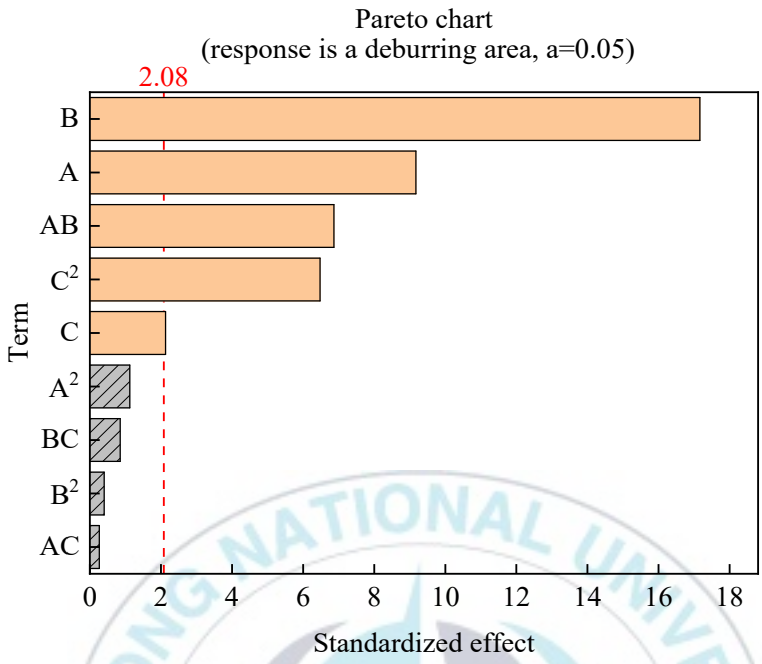

Fig. 4.1 Pareto chart of each term

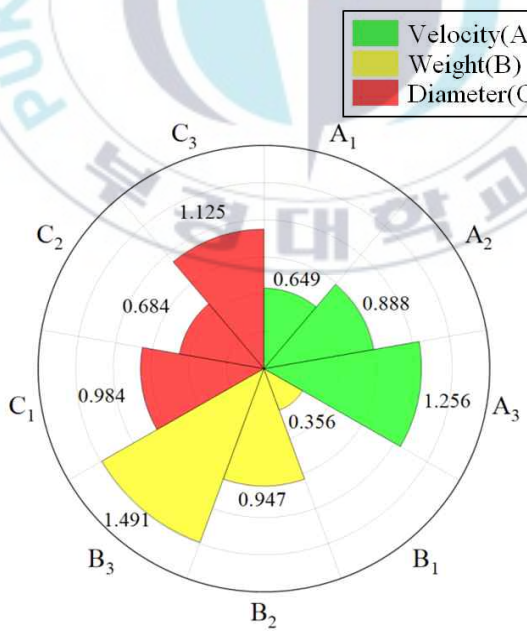

Fig. 4.2 Main effect plot of each level and factor

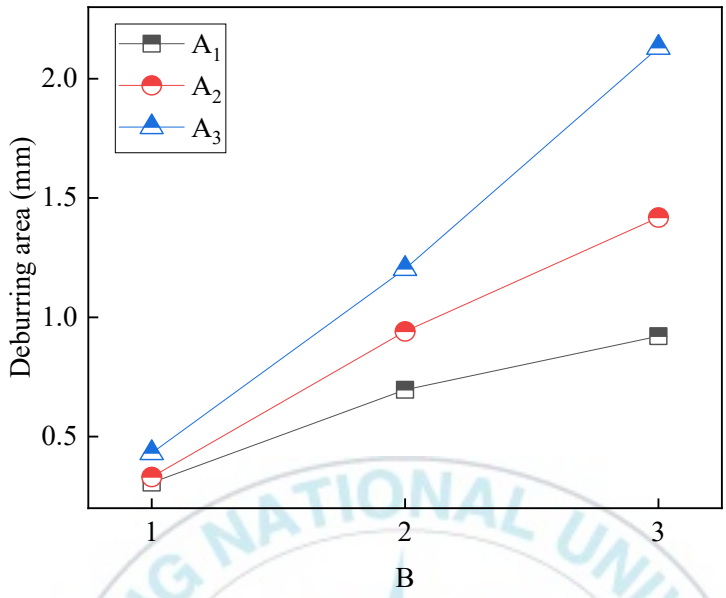

(a) Interaction between A and B factors

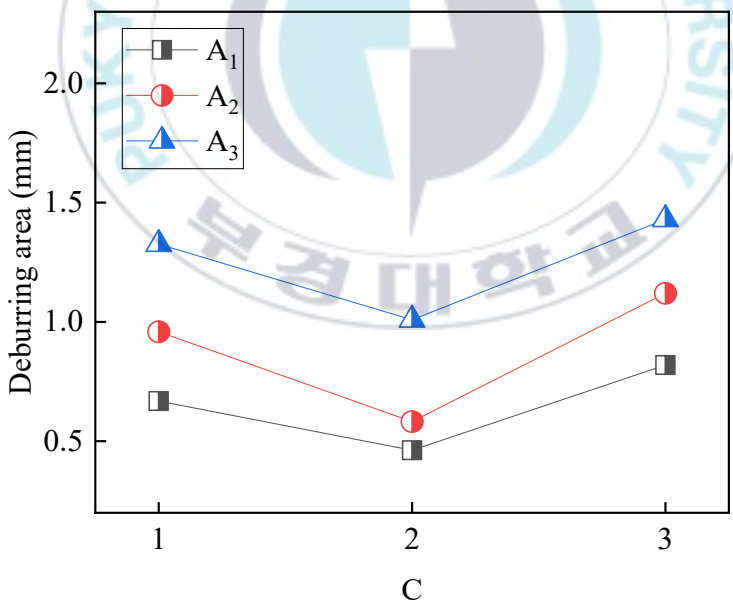

(b) Interaction between A and C factors

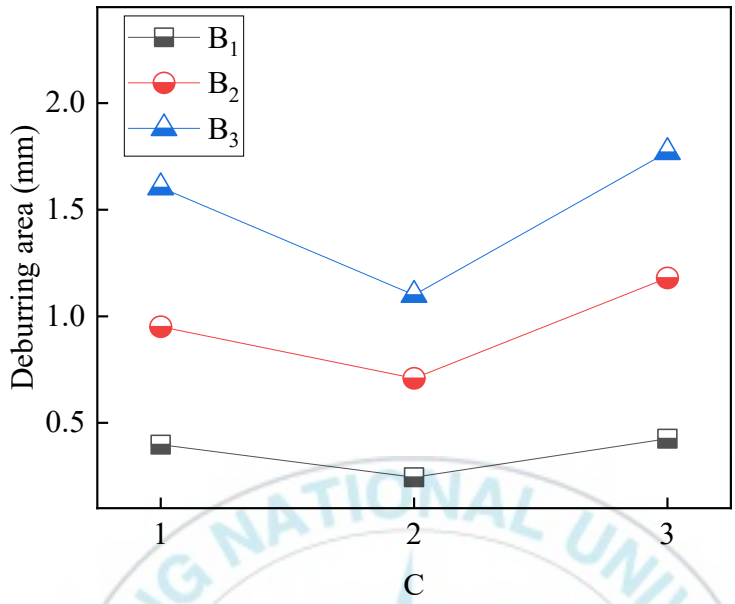

(c) Interaction between B and C factors

Fig. 4.3 Interaction plot of all combinations

PUKYONG NATIONAL UNIVERSITY
부경대학교

Table 4.1 ANOVA table of deburring

Terms	DF	SS	MS	F-value	P-value
A	1	1.655	1.655	84.140	0.000
B	1	5.794	5.793	294.460	0.000
C	1	0.089	0.089	4.540	0.045
C^2	1	0.825	0.825	41.930	0.000
AB	1	0.928	0.928	47.170	0.000
Error	21	0.413	0.020		
Total	26	9.705			

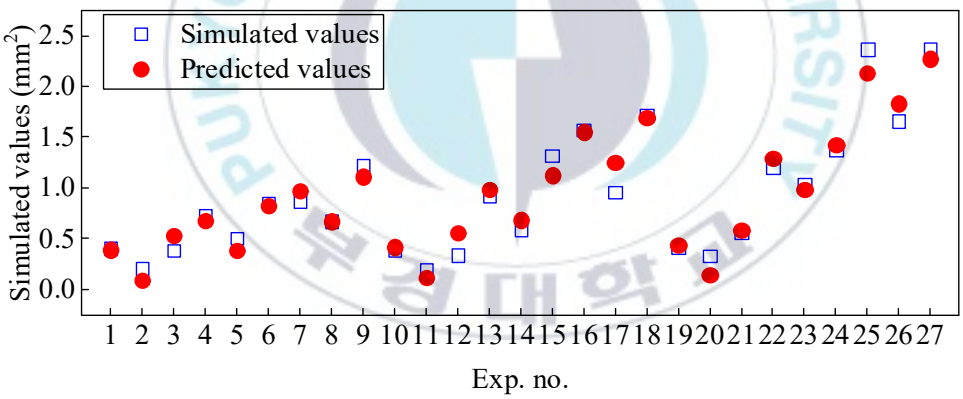

Fig. 4.4 Accuracy between simulated and predicted values

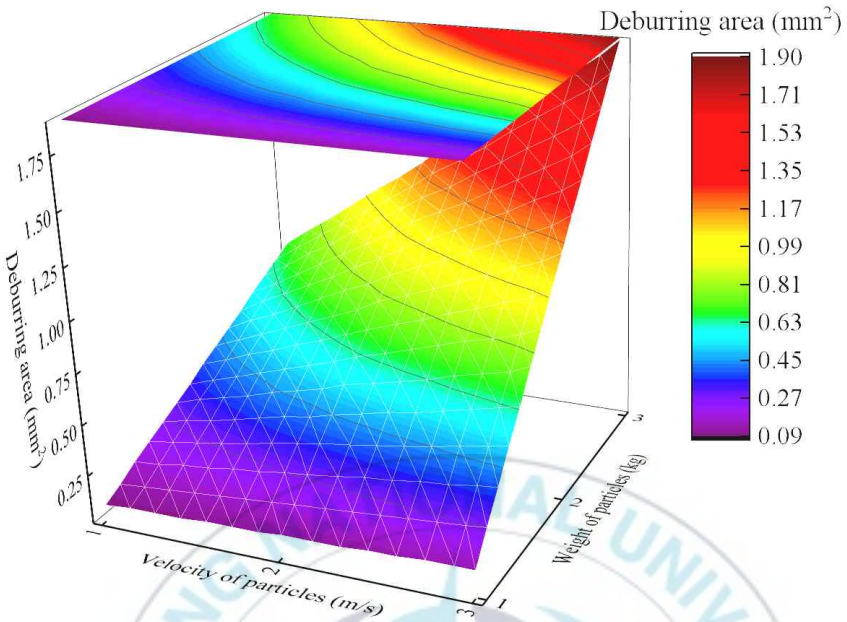

(a) Combination between A and B factors

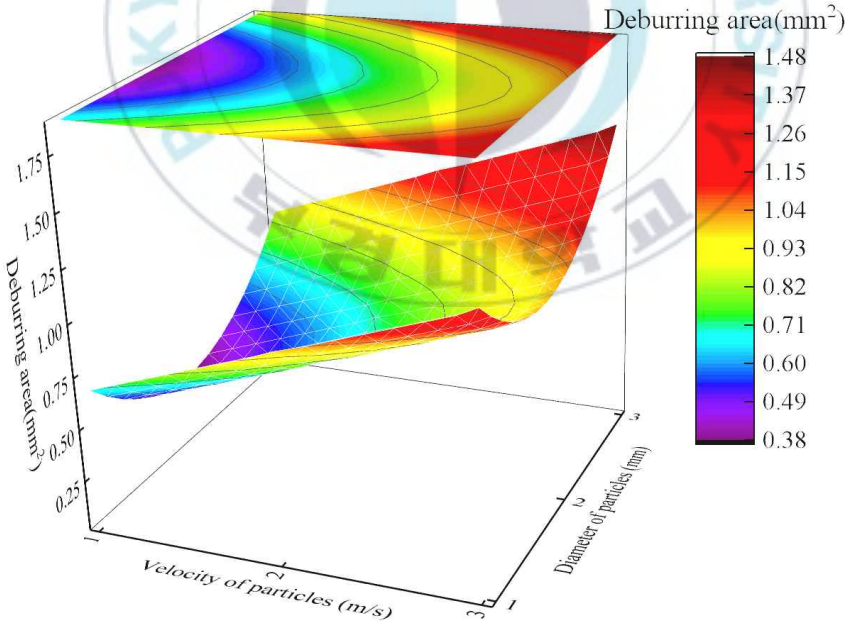

(b) Combination between A and C factors

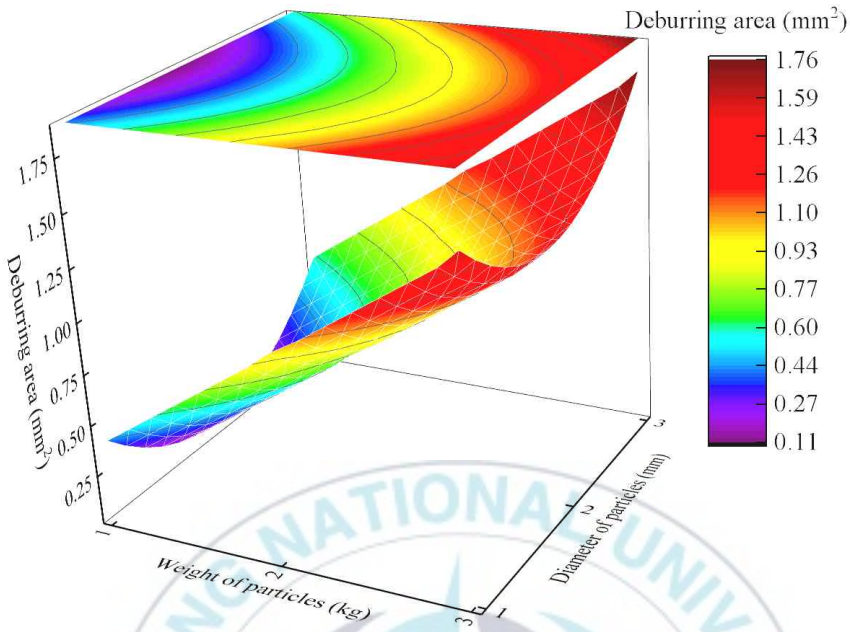

(c) Combination between B and C factors

Fig. 4.5 Response surface plots for process factors

PUKYONG NATIONAL UNIVERSITY
부경대학교

4.2 Experiment for removing burrs in micro precision parts

To validate the reliability of the numerical method, an evaluation for REMF was carried out. Photo. 4.2.1 was a set of equipment(EMD-850L, Amech. Co., Ltd., Korea) for REMF. The system was composed of container, magnetic, and motor control parts as mentioned chapter 2.1. The details of the machine were specified in Table 4.2. Moreover, the mechanical and chemical properties of materials ware listed in Table 4.3, Table 4.4, and Table 4.5.

Before REMF process, the burrs were formed around the edges of workpiece as represented in Fig. 4.6, because the specimen was slotted by a milling machine. The burr heights were measured using the contour measuring instrument(CV-3200, Mitutoyo, Japan) as shown in Photo. 4.2.2.

The factors and levels were listed in Table 4.6 in accordance with the factors as mentioned in chapter 3.2. Table 4.7 showed the designed experiments by $L_9(3^4)$ Taguchi orthogonal array to reduce a burden of operating cost and time.

For the quantitative analysis, variances of the deburring effect were computed as the relative ratio for burr height. The relative ratio for burr height(r_H) was defined as Eq. (4.2).

$$r_H = \frac{B_f}{B_i} \tag{4.2}$$

where B_i was a initial burr height and B_f was a final burr height

afterwards on REMF. When r_H was close to 0, it proved that the superior performance of deburring was achieved, since the effective abrasive process showed that the burr height remains almost zero.

Signal-to-noise ratio(S/N ratio) proved the desired signal to the background noise. It was calculated by the-smaller-the-better to estimate the optimal combination of experimental factors because the smaller r_H yield the better performance. The characteristic was used for the smaller S/N ratio by following Eq. (4.2)[40].

$$\eta = -10\log\left(\frac{1}{n}\sum_{1}^{n} y_i^2\right) \tag{4.2}$$

where y_i was the value of response and n was the number of experiments.

Differences of the burr height were drawn in Fig. 4.7. The analysis of S/N ratio for each condition was described in Table 4.8 and Fig. 4.8. As the results, B factor of the particles' weight exerted strong effects on the elimination of burr, followed by C factor of the particles' diameter, and R factor of the particles' rotational velocity. The minimum value about 16.8 was obtained at $R_3B_2C_1$, which was 1,800 rpm of the rotational velocity, 1.5 kg of the weight, and 0.3 mm of the diameter.

Furthermore, the optimal combination of conditions correlated with r_H was $R_3B_2C_3$, which was 1,800 rpm, 1.5 kg, and 0.7 mm. The optimal response of r_H was 14.4. Compared between the minimum and optimal results, the relative ratio of burr height reduced by 14.3%.

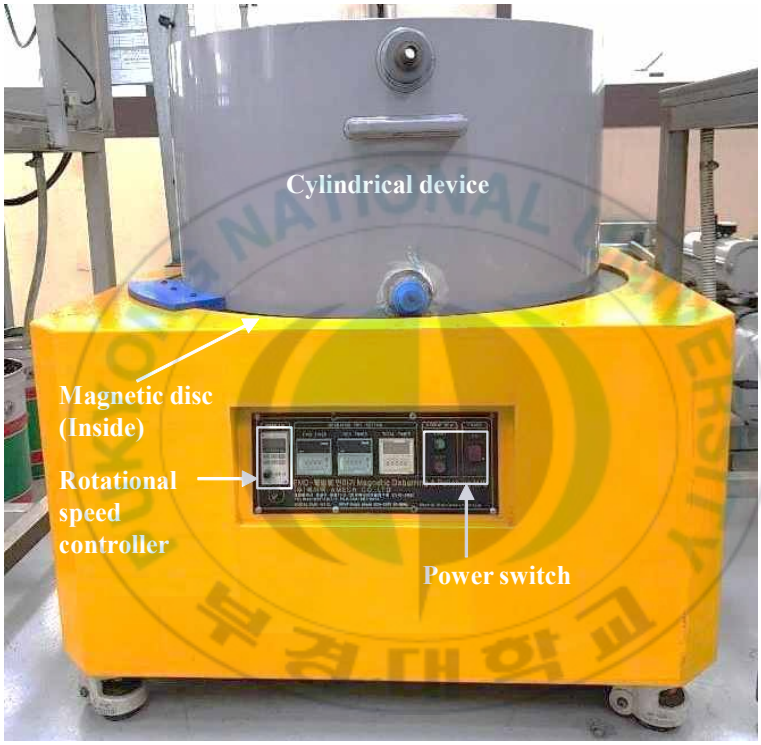

Photo. 4.1 Machine for REMF

Table 4.2 Specification of the equipment

Items		Values
Model		EMD-850L
Dimension(mm^3)		980×980×640
Parts container(mm^3)		ϕ750×300
Weight(kg)		215
Motor AC(Kw)		3.75
Speed of revolution(rpm)		300~1,800
Maximum operating time(min)		100
Power	Voltage range(V)	110~230
	Frequency(Hz)	10~60
	Type	Inverter control
	Phase	3
Magnets	Material	Nd-Fe-B
	The number of poles	4
	Maximum magnetic density(mT)	68

Table 4.3 Properties of Al6061 and STS304

Materials	Mechanical properties	
Al6061	Density(kg/m^3)	2,700
	Yield strength(MPa)	276
	Tensile strength(MPa)	310
	Shear strength(MPa)	207
	Poisson's ratio	0.33
	Elongation(%)	17
STS304	Density(kg/m^3)	8,000
	Yield strength(MPa)	205
	Tensile strength(MPa)	515
	Shear strength(MPa)	77,000
	Poisson's ratio	0.29
	Elongation(%)	40
	Volume magnetic susceptibility	2.2

Table 4.4 Chemical composition(wt. %) of Al6061

Cr	Cu	Fe	Mg	Mn	Si	Ti	Zn
0.195	0.275	0.700	1.000	0.150	1.200	0.150	0.250

Table 4.5 Chemical composition(wt. %) of STS304

C	Cr	Fe	Mn	Ni	Si	P	S
0.080	19.000	70.173	2.000	9.250	1.000	0.045	0.030

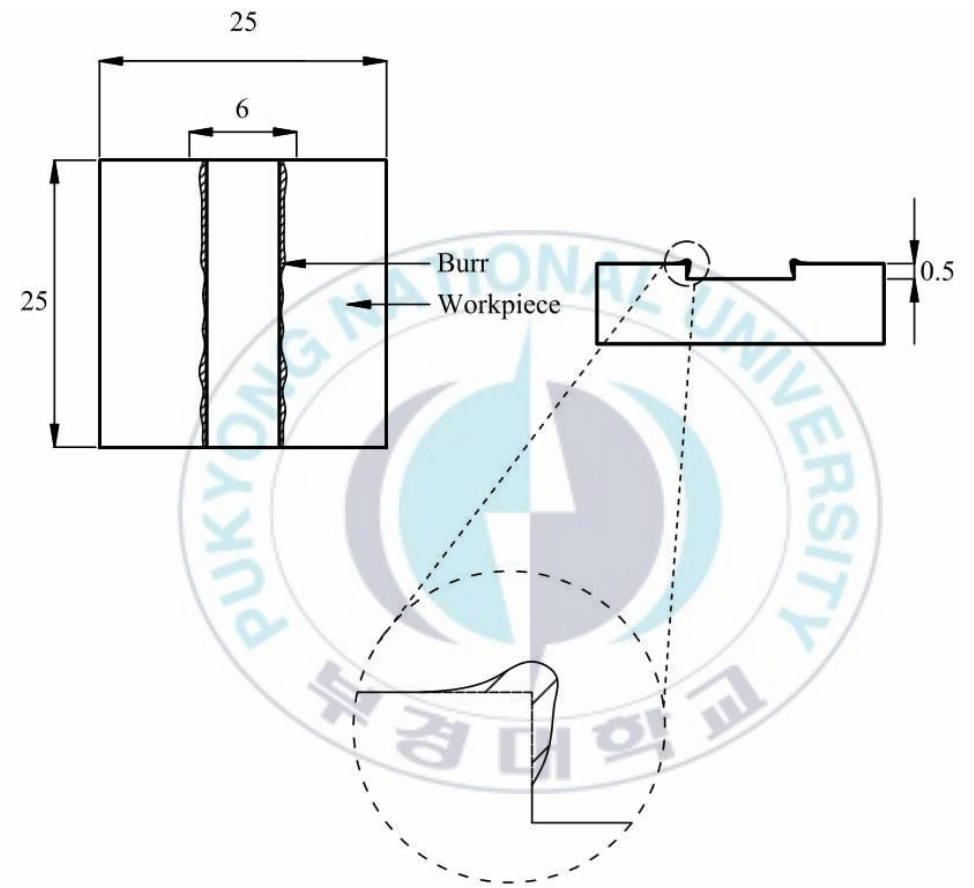

Fig. 4.6 The configuration of the workpiece

Photo. 4.2 Contour measuring instrument of CV-3200

Table 4.6 Factors and levels of experiment

Factors	Levels		
	1	2	3
Rotational velocity of particles(rpm), R	1,200	1,500	1,800
Weight of particles(kg), B	1.0	1.5	2.0
Diameter of particles(mm), C	0.3	0.5	0.7

Table 4.7 Taguchi array $L_9(3^4)$ for REMF

Exp. no.	Levels		
	R	B	C
1	1	1	1
2	1	2	2
3	1	3	3
4	2	1	2
5	2	2	3
6	2	3	1
7	3	1	3
8	3	2	1
9	3	3	2

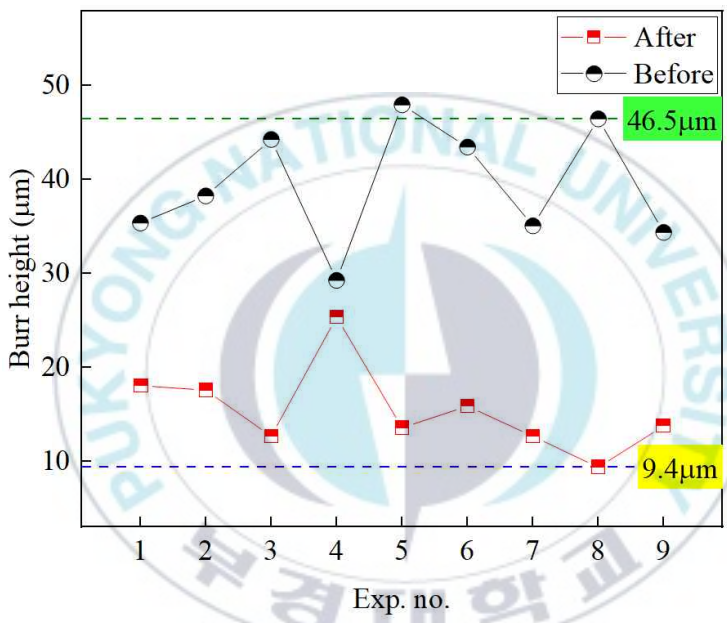

Fig. 4.7 The difference of burr height

Table 4.8 Response for S/N ratio of r_H

Levels	S/N ratio		
	R	B	C
1	10.833	9.204	12.117
2	10.417	12.889	9.185
3	12.627	11.783	12.574
Difference	2.210	3.685	3.388
Rank	3	1	2

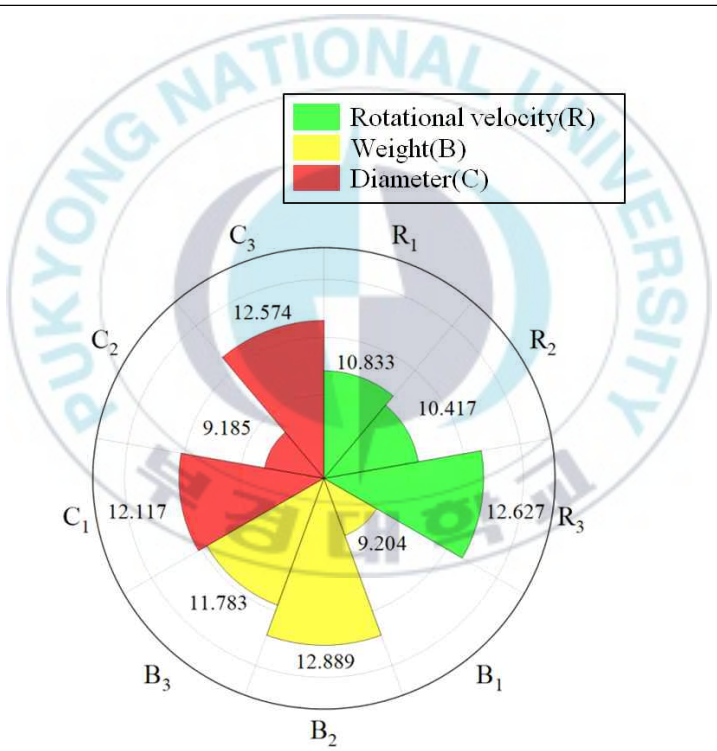

Fig. 4.8 Main effects for S/N ratio of r_H

4.3 Results and discussions

In this chapter, the analysis of chapter 4.1 and chapter 4.2 could be summarized as follows.

The effects of the suggested process were analyzed using the second-order regression model and ANOVA. The fitting model was derived with the interaction term between A factor of the particles' velocity and B factor of the particles' weight, as well as the square term of C factor of the particles' diameter. The influential condition of the differences was B factor, followed by A and C factor. The optimal combination affecting the maximum effective deburring area was $A_3B_3C_3$, corresponding to 33 m/s of the velocity, 2.0 kg of the weight, and 0.7 mm of the diameter, respectively. The reliable model attained a good-agreement with measurements and the accuracy of predictive values, 95.7% and 83.3% respectively.

Moreover, the deburring effect of REMF was explored by means of the experimental method. The examination was designed using Taguchi array as the effective statistic strategy. The burr heights were measured to evaluate r_H and the significances were derived by S/N ratio, based on the-smaller-the-better. B factor of the particles' weight dominantly influenced the response, followed by C of the particles' diameter and R factor of the particles' rotational velocity. The minimum measurement was achieved around 16.8 at $R_3B_2C_1$ of the experimental no. 8, which was 1,800 rpm of the rotational velocity, 1.5 kg of the weight, and 0.3 mm of the diameter. On the other hand, the optimal value was about 14.4 at $R_3B_2C_3$, which was 1,800 rpm, 1.5 kg, and 0.7 mm. The optimal value of r_H was reduced

approximately 14.3% in comparison to the minimum experimental outcome.

The optimal conditions of each approach were shown in Fig. 4.9. From these results, it was noted that there was the discrepancy between the outcomes obtained by simulated and actual methods. The reason why B factor in the virtual approach considered only a conflict between the particle and the surface in the limited tiny area. However, both particle-surface and particle-particle collisions affected the performance of REMF in practical. In these respects, the number of involved particles increased at the heavier particles' weight. As a result, motion of magnetized particles restricted to improve the process efficiency due to the interaction each other.

Although these results had few differences, the similar tendency of the optimal factors was observed. The optimal levels of A and C factor were identical with each method. And the most influential factor was B factor for both strategies. In addition, C factor had the similar quadratic curve in respective main effect plots. Thus, the numerical prediction was the reliable estimation for improving burr removal rate.

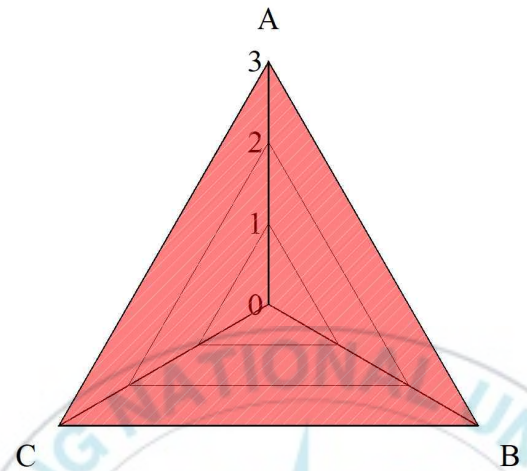

(a) Optimal condition of numerical method

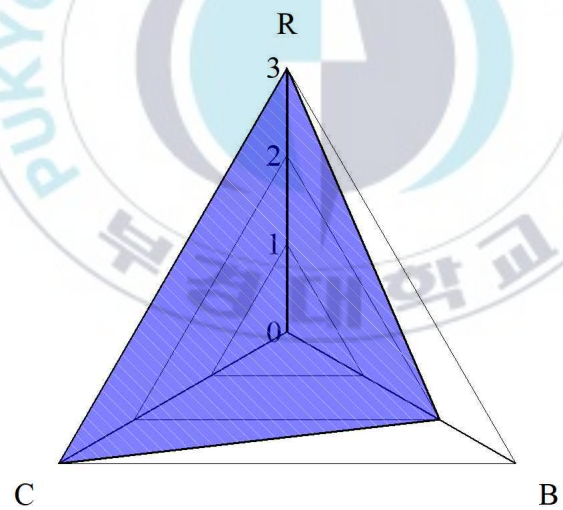

(b) Optimal combination of experimental results

Fig. 4.9 The comparison with results of each optimization

5. Conclusions

In this paper, REMF process was suggested to remove undesired parts on freeform geometry. In order to clarify the effect of REMF on burr reduction, numerical analyses of stress distribution on the workpiece in variable machining parameters were analyzed using explicit dynamic FEA based on full factorial design. According to the simulated results above yield stress, available deburring areas were extracted. In addition, the predictive model was developed by RSM. It was clear that the numerical method were reliable compared to experimental outcomes. As the results, following summarization was obtained.

(1) In simulated results of single magnetized particle, the effective stress on the surface which affected burr reduction was proportionally influenced by particle's velocity, diameter, and tilt angle. Based on the stress distributions of single collision, evaluations of multiple particles were performed with random kinetic characteristics to obtain reliable deburring effect close to real one. Consequently, the optimal condition was $A_3B_3C_3$, which was 33 m/s of the velocity, 2.0 kg of the weight, and 0.7 mm of the diameter. From the ANOVA, the most dominant property was particles' weight, followed by particles' diameter and velocity with the confidence levels of 0.05.

(2) The predictive model was developed by RSM. Its goodness-of-fit and

accuracy of predictive values were about 95.7% and 83.3%, respectively. The similarity of the predictive model which had deburring area of 2.27 mm^2, was about 95.4% compared to the simulated optimum results about 2.38 mm^2.

(3) In accordance with experimental results, the minimum condition was $R_3B_2C_1$ corresponding to 1,800 rpm of the rotational velocity, 1.5 kg of the weight, and 0.3 mm of the diameter based on the-smaller-the-better characteristics of S/N ratio. As the result of Taguchi optimization method, the optimal process was $R_3B_2C_3$, which was 1,800 rpm, 1.5 kg, and 0.7 mm. Comparison between the minimum and optimal conditions, the relative ratio for burr height was significantly reduced by 14.4%.

(4) The determined conditions of two different strategies were compared to validate reliability of simulated results. As the results, the suggested numerical model relatively showed the consistency. Therefore, it was proved that the simulated approach is valid to verify the effect of REMF on improving process efficiency. Furthermore, investigations considering the disturbing effect of the particle-particle interaction could be advanced with the improved accuracy.

REFERENCES

1. F. Hashimoto, H. Yamaguchi, P. Krajnik, K. Wegener, R. Chaudhari, H. W. Hoffmeister, and F. Kuster, “Abrasive fine-finishing technology”, CIRP annals, Vol. 65, No. 2, pp. 597-620, 2016.
2. Y. Feng, J. Ren, and Y. Liang, “Prediction and reconstruction of edge shape in adaptive machining of precision forged”, The International Journal of Advanced Manufacturing Technology, Vol. 96, No. 5-8, pp. 2355-2366, 2019.
3. V. K. Jain, “Abrasive-based nano-finishing techniques: an overview”, Machining science and technology, Vol. 12, No. 1, pp. 257-294, 2008.
4. T. W. Kim, and J. S. Kwak, “A study on deburring of magnesium alloy plate by magnetic abrasive polishing”, International Journal of Precision Engineering and Manufacturing, Vol. 11, No. 2, pp. 189-194, 2010.
5. L. Nagdeve, V. K. Jain, and J. Ramkumar, “Nanofinishing of freeform/ sculptured surfaces: state-of-the-art”, Manufacturing review, Vol. 5, No. 6, pp. 1-20, 2018.
6. V. K. Jain, and S. G. Adsul, “Experimental investigations into abrasive flow machining”, International Journal of Machine Tools and Manufacture, Vol. 40, No. 7, pp. 1003-1021, 2000.
7. M. R. Sankar, V. K. Jain, and J. Ramkumar, “Rotational abrasive flow finising(R-AFF) process and its effects on finished surface topography”, International Journal of Machine Tools and Manufacture, Vol. 50, No. 7, pp. 637-650, 2010.
8. D. P. Tan, S. M. Ji, and Y. Z. Fu, “An improved soft abrasive flow

finishing method based on fluid collision theory", The International Journal of Advanced Manufacturing Technology, Vol. 85, No. 5-8, pp. 1261-1274, 2016.

9. V. K. Jain, S. C. Jayswal, and P. M. Dixit, "Modeling and simulation of surface roughness in magnetic abrasive finishing using non-uniform surface profiles", Materials and Manufacturing Processes, Vol. 22, No. 2, pp. 256-270, 2007.
10. H. Yamaguchi, and J. Kang, "Study of ferrous tools in internal surface and edge finishing of flexible capillary tubes by magnetic abrasive finishing", Transaction of NAMRI/SEM, Vol. 38, No. 1, pp. 177-184, 2010.
11. P. Kala, V. Sharma, and P. M. Pandey, "Surface roughness modelling for double disk magnetic abrasive finishing process", Journal of Manufacturing Processes, Vol. 25, No. 1, pp. 37-48, 2017.
12. X. Sun, and Y. Zou, "Development of magnetic abrasive finishing combined with electrolytic process for finishing SUS304 stainless steel plane", The International Journal of Advanced Manufacturing Technology, Vol. 92, No. 9-12, pp. 3373-3384, 2017.
13. M. G. Patil, K. Chandre, and P. S. Misra, "Magnetic abrasive flow finishing: A review", Advanced Materials Research, Vol. 418, No. 1, pp. 1577-1581, 2012.
14. M. R. Sankar, J. Ramkumar, and V. K. Jain, "Experimental investigation and mechanism of material removal in nano finishing of MMCs using abrasive flow finishing process", Wear, Vol. 266, No. 7-8, pp. 688-698, 2009.
15. H. S. Gang, T. H. Kim, and J. S. Kwak, "Control of polarity by magnetic

array table in magnetic abrasive polishing process", Transaction of the Korean Society of Mechanical Engineers-A, Vol. 34, No. 11, pp. 16443-1648, 2010.

16. J. S. Kwak, "Mathematical model determination for improvement of surface roughness in magnetic-assisted abrasive polishing of nonferrous AISI316 material", Transaction of Nonferrous Metals Society of China, Vol. 22, pp. s845-s850, 2012.
17. M. Sarkar, and V. K. Jain, "Nanofinishing of freeform surfaces using abrasive flow finishing process", Proceedings of the Institution of Mechanical Engineers-Part B: Journal of Engineering Manufacture, Vol. 231, No. 9, pp. 1501-1515, 2017.
18. Y. C. Jung, Effect of polishing time of surface roughness and surface topography on Co-Cr alloy by dental auto polishing system, Master's thesis, Catholic University of Pusan Dental Laboratory Science, 2020.
19. M. S. Cheema, G. Venkatesh, A. Divivedi, and A. K. Sharma, "Developments in abrasive flow machining: a review on experimental investigations using abrasive flow machining variants and media", Proceedings of the Institution of Mechanical Engineers, Part B: Journal of Engineering Manufacture, Vol. 226, No. 1, pp. 1951-1962, 2012.
20. L. Heng, Y. J. Kim, and S. D. Mun, "Review of superfinishing by the magnetic abrasive finishing process", High Speed Machining, Vol. 3, No. 1, pp. 42-55, 2017.
21. C. Wang, C. F. Cheung, L. T. Ho, K. L. Yung, and L. Kong, "A novel magnetic field-assisted mass polishing of freeform surface", Journal of Manufacturing Processing Technology, Vol. 279, No. 1, pp. 1-9, 2020.

22. V. K. Gorana, V. K. Jain, and G. K. Lai, “Experimental investigation into cutting forces and active grain density during abrasive flow machining”, International Journal of Machine Tools and Manufacture, Vol. 44, No. 2-3, pp. 201-211, 2004.
23. V. K. Gorana, V. K. Jain, and G. K. Lai, “Prediction of surface roughness during abrasive flow machining”, The International Journal of Advanced Manufacturing Technology, Vol. 31, No. 3-4, pp. 258-267, 2006.
24. Y. Seifu, S. S. Kumar, and S. S. Hiremath, “Modeling and simulation: machining of mild steel using indigenously developed abrasive flow machine”, Procedia Technology, Vol. 25, No. 1, pp. 1312-1319, 2016.
25. H. Yamaguchi, and T. Shinmura, “Study of an internal magnetic abrasive finishing using a pole rotation system: Discussion of the characteristic abrasive behavior”, Precision Engineering, Vol. 24, No. 3, pp. 237-244, 2000.
26. G. W. Ghang, B. H. Yan, and R. T. Hsu, “Study on cylindrical magnetic abrasive finishing using unbonded magnetic abrasives”, International Journal of Machine Tools and Manufacture, Vol. 42, No. 5, pp. 575-583, 2002.
27. S. L. Ko, Y. M. Baron, and J. I. Park, “Micro duburring for precision parts using magnetic abrasive finishing method”, Journal of Materials Processing Technology, Vol. 187, No. 1, pp. 19-25, 2007.
28. R. S. Mulik, and P. M. Pandey, “Experimental investigations and optimization of ultrasonic assisted magnetic abrasive finishing process”, Proceedings of the Institution of Mechanical Engineers-Part B: Journal of Engineering Manufacture, Vol. 225, No. 8, pp. 1347-1362, 2011.
29. M. Kumar, S. Singh, and H. Farwaha, “Optimization and prediction of

sintering process parameters for magnetic abrasives preparation using response surface methodology", International Journal of Data and Network Science, Vol. 3, No. 2, pp. 103-108, 2019.

30. A. M. Wani, V. Yadava, and A. Khatri, "Simulation for the prediction of surface roughness in magnetic abrasive flow finishing,", Journal of Materials Processing Technology, Vol. 190, No. 1-3, pp. 282-290, 2007.
31. P. Singh, L. Singh, and S. Singh, "Manufacturing and performance analysis of mechanically alloyed magnetic abrasives for magneto abrasive flow finishing", Journal of Manufacturing Processes, Vol. 50, No. 1, pp. 161-169, 2020.
32. T. Furuya, Y. Wu, M. Nomura, K. Shimada, and K. Yamamoto, "Fundamental performance of magnetic compound fluid polishing liquid in contact-free polishing of metal surface", Journal of Materials Processing Technology, Vol. 201, No. 1-3, pp. 536-541, 2008.
33. A. Azami, A. Azizi, A. Khoshanjam, and M. Hadad, "A new approach for nanofinishing of complicated-surfaces using rotational abrasive finishing process", Materials and Manufacturing Processes, Vol. 35, No. 8, pp. 940-950, 2020.
34. T. B. Jones, Electromechanics of particles, 1st Ed., Cambridge university press, cambridge, UK, 1995.
35. K. Nishimura, T. Namiki, T. Ikeno, Y. Yamamoto, and W. D. Hutchison, "Magnetic and transport properties of stainless steels at low temperature", Acta Metallurgica Slovaca, Vol. 23, No. 3, pp. 257-263, 2017.
36. H. Yamagughi, T. Shinmura, and M. Takenaga, "Development of a new

precision internal machining process using an alternating magnetic field", Precision Engineering, Vol. 27, No. 1, pp. 51-58, 2003.

37. H. Kumar, S. Singh, and P. Kumar, "Surface finishing and modification of brass tube by magnetically assisted cold worked stainless steel pins", Journal of Tribology and Surface Engineering, Vol. 3, No. 3-4, pp. 187-202, 2012.
38. M. Yoshioka, S. Hira, and H. Takeuchi, Motion of magnetic barrel media in rotary magnetic field, Abrasive Technology: Current Development and Applications I, pp. 469-474, 1999.
39. D. Steinberg, Equation of State and Strength Properties of Selected Materials, Lawrence Livermore National Laboratory, Livermore, USA, 1991.
40. F. Kahraman, and B. Sugözü, "An integrated approach based on the Taguchi method and response surface methodology to optimize parameter design of asbestos-free brake pad material", Turkish Journal of Engineering, Vol. 3, No. 3, pp. 127-132, 2019.